NASA-CR-159423

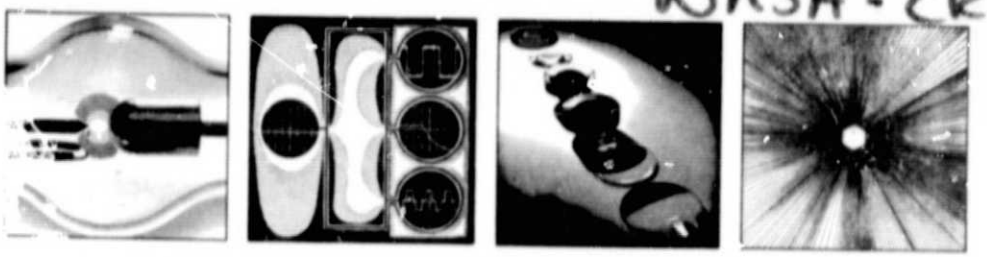

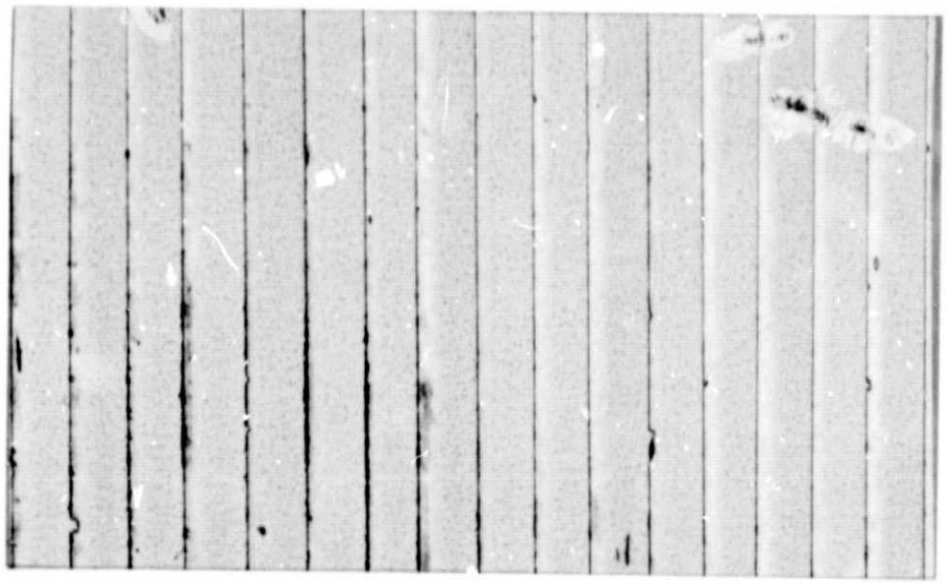

(NASA-CR-159423) INERT GAS ION SOURC PROGRAM Final Report, 2 Mar. 1977 - Jan. 1978 (Xerox Electro-Optical Systems, Pasadena) 76 p HC A05/MF A01 CSCL 21C

N79-10120

Unclas
G3/20 33813

XEROX

Final Report

INERT GAS ION SOURCE PROGRAM

Prepared for:

National Aeronautics and Space Administration
Lewis Research Center
21000 Brookpark Road
Cleveland, Ohio 44135

Contract NAS3-20393

XEOS Report 2361-Final July 13, 1978

Prepared by:
Project Staff

Approved by:

Rex L. Waddell, Manager
Electronic Systems Division

Xerox Electro-Optical Systems

300 North Halstead Street
Pasadena, California 91107

1. Report No.	2. Government Accession No.	3. Recipient's Catalog No.
CR-159423		

4. Title and Subtitle	5. Report Date
INERT GAS ION SOURCE PROGRAM	July 1978
	6. Performing Organization Code

7. Author(s)	8. Performing Organization Report No.
William D. Ramsey	
	10. Work Unit No.

9. Performing Organization Name and Address	11. Contract or Grant No.
Xerox Electro-Optical Systems 300 N. Halstead Pasadena, California 91107	NAS 3-20393

12. Sponsoring Agency Name and Address	13. Type of Report and Period Covered
National Aeronautics and Space Administration Lewis Research Center 21000 Brookpark Road Cleveland, Ohio 44135	Final March 2, 1977 to Report January 2, 1978
	14. Sponsoring Agency Code

15. Supplementary Notes

Project Manager: Shigeo Nakanishi, NASA-Lewis Research Center, Cleveland, Ohio

16. Abstract

The original 12 cm hexagonal magneto-electrostatic containment discharge chamber described by Moore in 1969 has been optimized for argon and xenon operation. Argon mass utilization efficiencies of 65 to 77 percent were achieved at keeper-plus-main discharge energy consumptions of 200 to 458 eV/ion, respectively. Xenon performance of 84 to 96 percent mass utilization was realized at 203 to 350 eV/ion. The optimization process and test results are discussed in the report.

17. Key Words (Suggested by Author(s))	18. Distribution Statement
Electric Propulsion Argon & Xenon Ion Source 12 cm Ion Thruster	Unclassified - Unlimited

19. Security Classif. (of this report)	20. Security Classif. (of this page)	21. No. of Pages	22. Price*
Unclassified	Unclassified	73	

*For sale by the National Technical Information Service, Springfield, Virginia 22161

NASA-C-168 (Rev. 10-75)

CONTENTS

CONTENTS (Contd)

ILLUSTRATIONS

SECTION 1

INTRODUCTION

The changing requirements of space propulsion systems, particularly for large space vehicles and high specific impulse missions, have pointed up the need for efficient inert gas thrusters. The inherent compatibility of an inert gas propellant and its expanding plume with spacecraft surfaces is obvious. The available supply and negligible environmental impact of inert gas propellants are also significant reasons for their use in large space systems. Aside from space propulsion, applications of efficient inert gas ion sources to terrestrial uses such as etching, polishing, micromachining, and sputter coating have been identified.

The work described in this report was performed under Contract NAS3-20393, "Inert Gas Ion Source Development," administered by NASA Lewis Research Center. The report describes the modifications necessary to convert an existing magneto-electrostatic containment (MESC) discharge chamber to argon-xenon operation and the methods used to optimize its performance.

1.1 HISTORICAL ION SOURCE PERFORMANCE

Electrostatic ion thrusters have been developed primarily for cesium and mercury propellants. Sources and distribution of neutral and charged particle fluxes, their interaction with spacecraft, and possible corrective measures have been studied by several investigators.[1,2] Recently there has been considerable interest in inert gases, particularly xenon and argon, as propellants. Table 1-1 lists some pertinent parameters for the four leading propellants. Since thruster electrical performance is enhanced by high atomic weight and by low ionization

potential, xenon thruster performance will tend to be somewhat lower than mercury or cesium thruster performance. Argon which has an appreciably lower atomic weight than xenon and a higher ionization potential, will have the lowest performance of the group.

TABLE 1-1

PROPELLANT CHARACTERISTICS

	Argon	Xenon	Cesium	Mercury
Atomic Weight	39.9	131.3	132.9	200.6
q/m, coul/kg (x 10^5)	24.2	7.4	7.3	4.8
Ionization Potential V_1	15.8	12.1	3.9	10.4
Ionization Potential V_2	27.6	21.2	25.1	18.8

A factor favoring the inert gas propellants is their relatively low charge exchange cross section. Surprisingly, perhaps, inert gas propellant storage appears not to be a problem; the ratio of propellant to tankage weight is as high as for cesium with one-third the propellant density.

It has been shown by a number of workers that electron bombardment thrusters perform satisfactorily using inert gases as propellants.[3,4,5] Studies indicate that the best technical choice for space propulsion applications is xenon.[6] Argon is a possible alternate propellant when cost is also considered. For purposes of perspective, historic data on xenon sources are compared with data on mercury and cesium sources in figure 1-1. As might be expected, the data for each propellant improve with time, and typical eV/ion values are arranged in the same order as the ionization potentials.

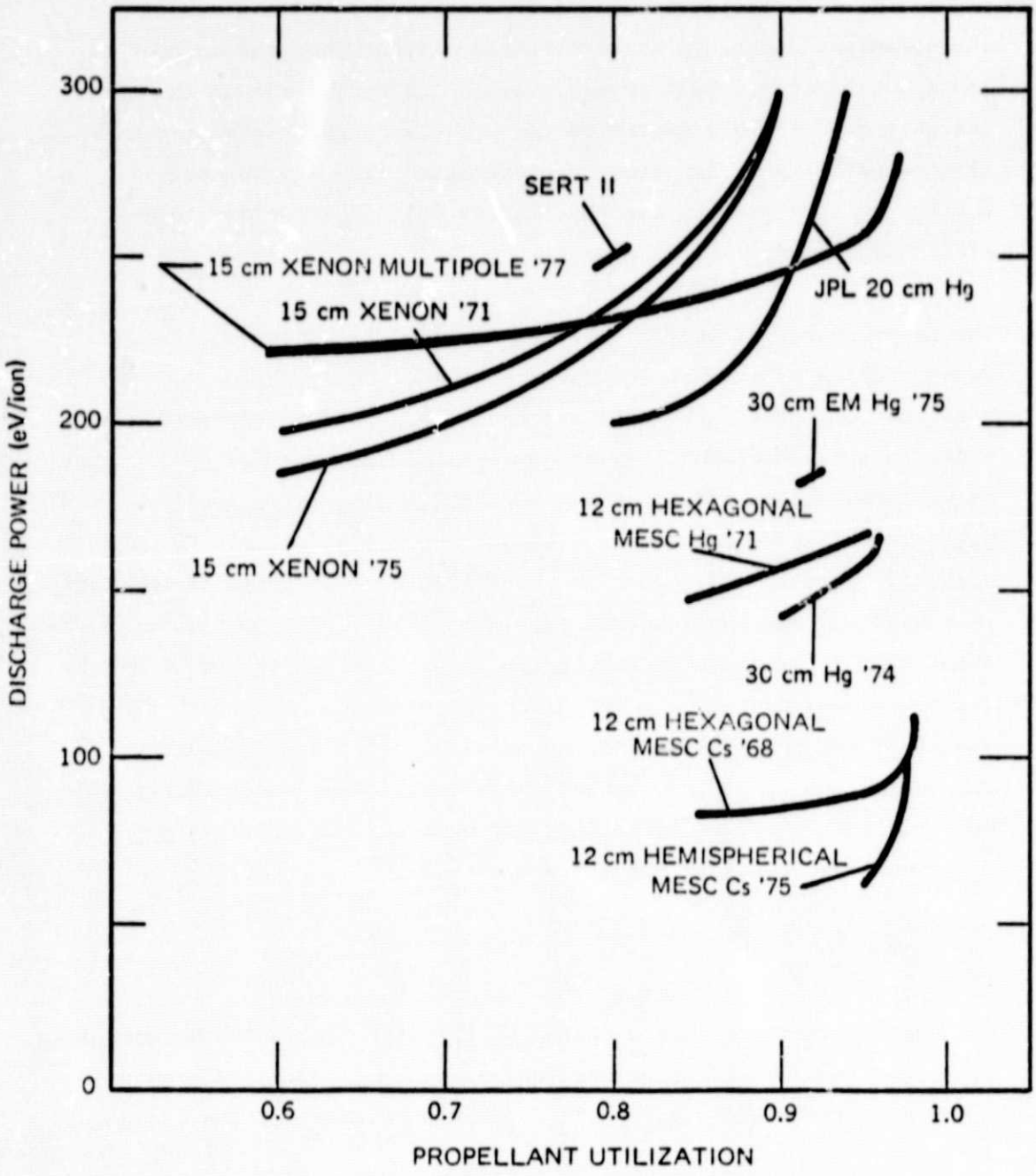

Figure 1-1. Historic Ion Thruster Performance

55273

1.2 ION SOURCE TECHNOLOGY

Electron bombardment ion thrusters use a Penning type discharge to ionize the thruster propellant flow. This propellant discharge is initiated and sustained by an electron current from the cathode to the anode structure that passes through the propellant in the discharge chamber. Ions generated in this discharge by electron collisions with propellant atoms are extracted from its downstream surface by accelerating electric fields which are applied to the electrode system.

The major source of inefficiency in the ionizing discharge is the recombination of ions on the walls of the discharge chamber. The ions that diffuse to the wall and recombine must be reionized in order to achieve high propellant mass utilization efficicency. The conventional means of minimizing ion wall losses is to apply an axial magnetic field to contain the plasma. The magnetic field forms a magnetic "bottle" that opens in the downstream direction of ion flow. This approach has two inherent problems. First, the magnitude of the axial magnetic field that can be applied is limited to low levels by the low plasma density and low discharge voltage. Secondly, the plasma is concentrated in the center of the discharge chamber by the JxB forces acting on the charged particles. These two problems combine to limit the mass efficiency and beam current density (mA/cm^2) a conventional thruster can achieve.

1.3 MESC ION SOURCE

The magneto-electrostatic containment thruster represents a radical departure from conventional thruster design and permits a significant increase in efficiency by providing a boundary at the discharge

chamber walls which reflects a large fraction of both ions and electrons approaching it. Ions are reflected by an electrostatic field at the boundary while electons are reflected by a magnetic field.

Another favorable aspect of the configuration is the low magnitude of the residual magnetic field within the discharge chamber plasma volume. Since the magnetic field or $\vec{J} \times \vec{B}$ force is the major cause of plasma density gradients at the screen electrode, the MESC technique provides a very uniform plasma density to allow efficient ion extraction with uniform geometry electrodes

The basic configuration of the magneto-electrostatic plasma containment boundary is shown in figure 1-2. The magnetic configuration is an array of magnetic pole strips where adjacent poles are of opposite polarity. All are backed with a common magnetically soft material and are maintained at the same potential as the thruster cathode. Between each pair of pole strips is an anode strip electrically isolated from the magnets.

Ionic wall losses are minimized by an unique interraction between the MESC geometry and discharge plasma that results in a reflective electrostatic potential at the plasma boundary. An electric field applied perpendicularly to a magnetic field ($\vec{E} \times \vec{B}$) produces a plasma drift velocity perpendicular to both. In the MESC design, the plasma near adjacent anodes drifts in opposite directions as the magnetic fields alternate in sense. Given the operational conditions, the discharge plasma viscosity is sufficient to retard the induced drift and to minimize the resultant counter EMF associated with it. This effect produces a plasma potential a few volts negative of the anodes that reflects the ions back into the discharge plasma.

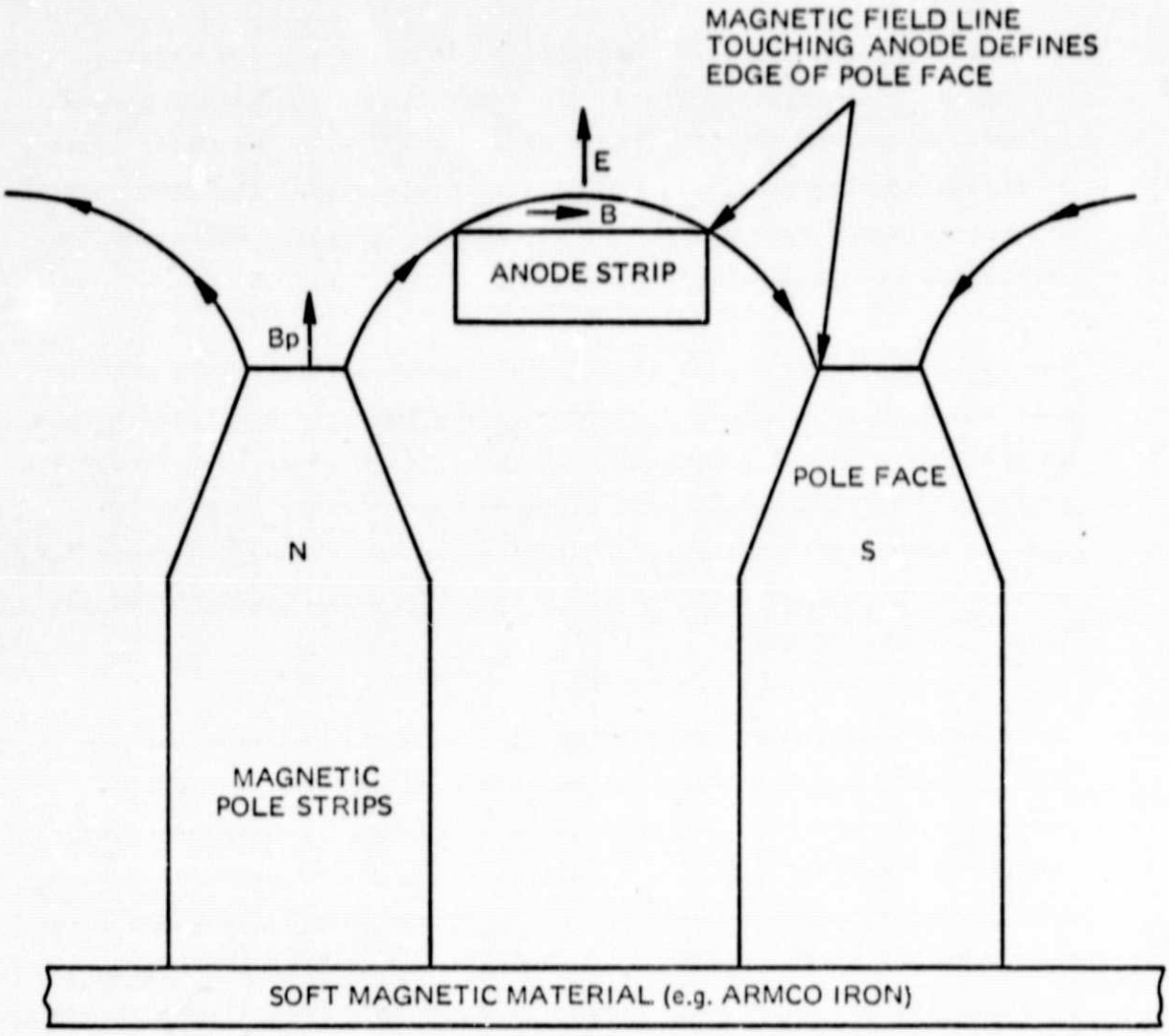

Figure 1-2. Basic MESC Configuration

39877

Plasma viscosity, φ, is mainly due to momentum transport by ions. The formula for viscosity is:

$$\varphi = 2.21 \times 10^{-16} \frac{T_+^{5/2} M_+^{1/2}}{\ln \alpha} \qquad \frac{\text{newton-sec}}{m^2}$$

where $\ln \alpha$ is a slowly varying function of Maxwellian electron temperature and plasma density referenced by Moore,[7] and T_+ and M_+ the ionic temperature and mass, respectively.

Discharge plasma electron losses are controlled by the magnetic and electrical field configuration within the discharge chamber. Since the magnets are at cathode potential, they are negative with respect to the discharge plasma and thus retard electron losses to the poles. Direct electron diffusion to the anodes is prevented by the transverse magnetic field between poles which causes the electron to undergo multiple collisions to reach the magnetic field lines joining the pole faces and the edges of the boundary anodes. Hence, the relative position of the magnet poles and anodes controls the electron current to the anodes. This position is an important parameter in thruster optimization.

The original MESC development was performed under NASA Contract NAS7-587 in 1968, using cesium as the propellant.[7] The original hardware was modified for operation with mercury under Intelsat Contract CSC-SS-189.[8] A smaller version was developed using cesium for flight on ATS-6[9] under NASA Contract NAS5-21192, and a 12 centimeter version was developed in flight prototype form under Intelsat Contract IS-452.[10]

As indicated in figure 1-1, some of the best ion source performance reported, as characterized by high propellant utilization and low energy consumption per ion extracted, have been achieved with this series of MESC thrusters.

1.4 ORGANIZATION OF THE REPORT

For clarity, this report has been divided into several sections. Section 2 discusses test apparatus, and Section 3 presents test results. Section 4 provides a summary.

SECTION 2

TEST APPARATUS

2.1 12 cm HEXAGONAL MESC ION SOURCE

2.1.1 MESC HEXAGONAL DISCHARGE CHAMBER DESIGN

The 12 cm hexagonal discharge chamber was the first designed to utilize the magnetoelectrostatic containment concept. Reduced to practice, MESC geometry is an array of alternating strip anodes and permanent magnets positioned orthogonally to the discharge chamber center line. The MESC pattern is repeated along the side of the chamber in hexagonally shaped rings of anodes and magnets. To maintain the same pattern on the rear wall, the alternating hex rings grow smaller in size approaching the chamber center line. The rear wall central region consists of a hollow cathode on axis situated inside the cathode pole magnet. The cathode pole magnet is a right circular cylinder 2.25 cm in diameter. A schematic of the discharge chamber is shown in figure 2-1.

The ARMCO iron discharge chamber walls complete the magnetic circuit between adjacent permanent magnet rings. Each hexagonal shaped magnet ring is composed of six bar magnets that are magnetized perpendicular to the discharge chamber wall. The AlNiCo magnets of each ring have the same polarity with fields of approximately 3500 gauss at the individual magnets in the direction of magnetization. The magnetic field sense alternates from ring to ring. As the fields of adjacent rings are equal and opposite, they tend to cancel over the major portion of the discharge chamber volume, thus limiting the significant field to the zone near the chamber walls. This field varies as an inverse function of radial displacement from the magnets. (See figure 1-2.)

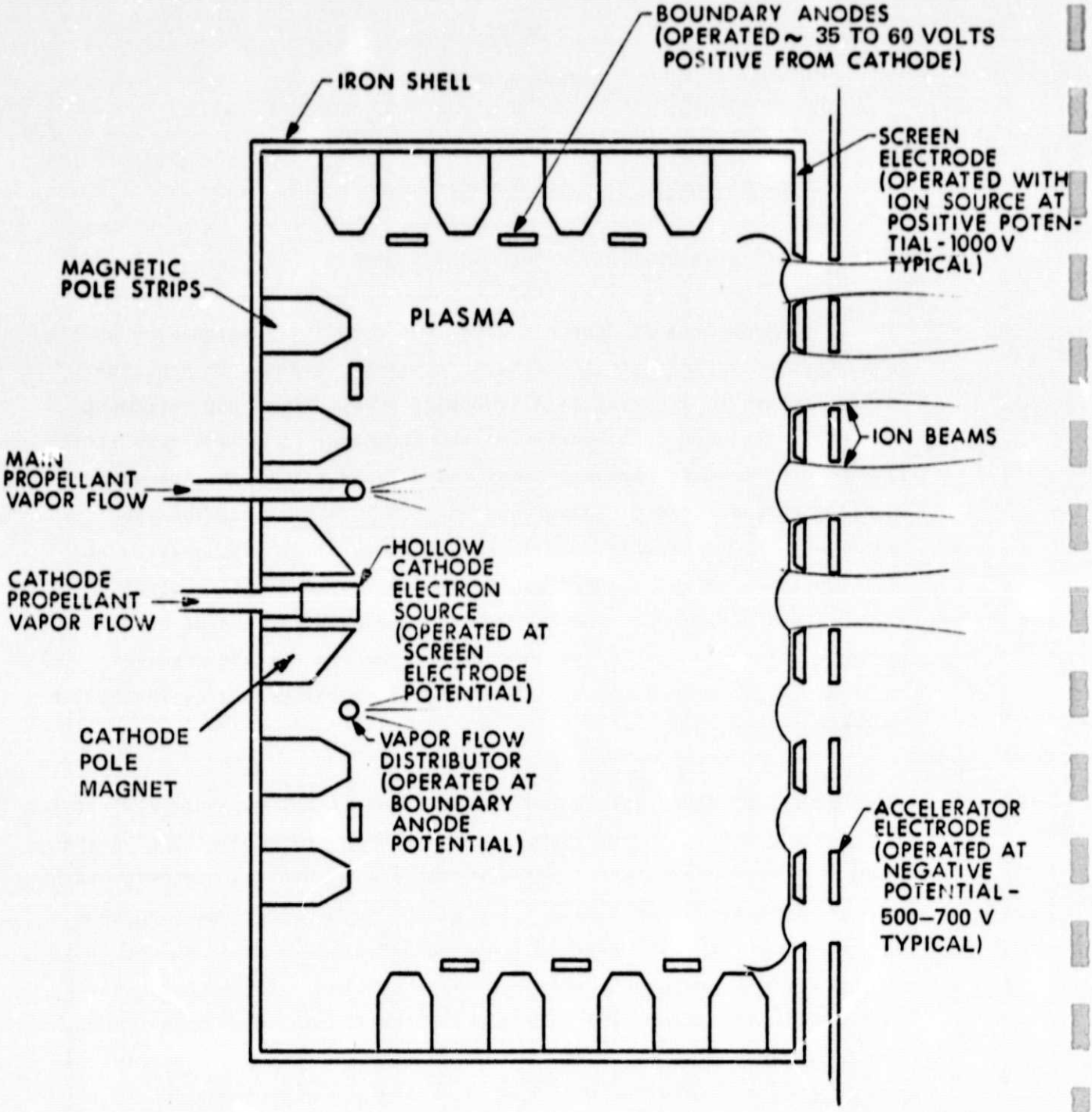

Figure 2-1. MESC Thruster Schematic

The positions of the anodes in this field are used to contain the discharge plasma ions and control the electron current to the boundary anodes.

The magnetic field terminates with an iron mirror piece on the downstream end of the discharge chamber. The mirror piece is attached to the chamber walls and functions as a virtual magnet next to the screen electrode.

Boundary andoes are interspersed between the hexagonal AlNiCo magnet rings to establish the MESC $\vec{E} \times \vec{B}$ field configuration at the edge of the discharge plasma region. The hexagonal shaped anode structures are made from 0.25 mm thick, non-magnetic stainless steel with a "U" cross section. Sides of the anode channel extended into the discharge region and are dimensioned to equalized anode electron current densities based on test data. In anode placemant, the item of importance is that portion of the anode that intercepts the critical magnetic field line. In this regard the top of the "U" and the edge of a flat anode are identical. (see figure 1-2). The anode "U" channel design facilitates radial position adjustments by changes in height of the "U" without removing the entire anode. It has been demonstrated with other propellants that the U-shaped design has the same operational characteristics as a flat anode strip at the same radial position in the magnetic field.

Details of the magneto-electrostatic boundary theory have been previously reported.[7] The theory found the boundary anode position in the magnetic field is a function of the general discharge plasma density, plasma temperature, and the plasma resistivity. Resistivity is a slowly varying function of plasma density and electron temperature. Boundary anode electron diffusion current is governed by the following relationship in a simplified two dimensional case.

$$J_D = \frac{\pi\, n^2 \nu k\, T_e}{B^2\, d} \qquad (2\text{-}1)$$

Where:

n = general discharge plasma density

ν = plasma resistivity

k = Boltzmann's constant

T = plasma temperature $(T = T^+ + T^-)$

B = Magnetic field parallel to the discharge chamber walls.

d = Center-to-center distance of the magnets

e = Electron charge

Reasonable mass utilization efficiency is usually found at discharge potentials approximately three times the propellant's first ionization potential. As the plasma temperature is determined by the propellant being tested, the magnetic field must be adjusted to compensate for the changes in anode current. This is accomplished by radial movement of the individual anode.

In principle it is possible to calculate optimum boundary anode radial position given the test gas plasma operational characteristics. Anode positions calculated by this method were found to approximate the placement necessary for optimum discharge chamber performance. Deviation between the calculated and actual locations probably resulted from using the simplified two dimensional case in deriving the diffusion current relationship. Actual anode positioning was an iterative process using test data to equalize anode-to-anode electron current densities with maximum mass utilization efficiency and minimum discharge power consumption (eV/ion).

Test gas was supplied to the discharge through the cathode and main feed ring plenum. Flow to the cathode was used primarily to control

the discharge electron current. Feed ring flow determined the ion beam current. The feed ring had sixty-one 0.32 mm diameter holes drilled in its downstream surface to distribute the main gas flow uniformly into the discharge chamber. The plenum also functioned as a boundary anode between the cylindrical cathode pole magnet and the next larger hexagonal magnet.

The cathode, cathode baffle structure, magnets, chamber walls and screen grid were tied together electrically to operate at positive high voltage, V^+. The feed ring operated at anode potential.

2.1.2 HOLLOW CATHODE SUBASSEMBLY

The inert gas hollow cathode subassembly used in testing was composed of three component parts designed to fit the inside diameter of the cathode pole magnet. A 3.2 mm diameter cathode on axis was encircled by a 1.1 cm diameter stainless steel keeper electrode support tube that was enclosed in a 1.6 cm diameter stainless steel baffle disk support tube. Tubes were used to support the keeper electrode and baffle disk as well as provide heat shielding between the cathode and cathode pole magnet. Boron nitride sleeves were used for electrical isolation between the keeper support tube and other hardware. The cathode subassembly is shown in figure 2-2.

2.1.2.1 Inert Gas Hollow Cathode

The inert gas hollow cathode was similar to the most recent mercury cathode designs described in the literature.[11] The orifice plate was a 2 percent thoriated tungsten disk that was countersunk half its thickness and electron beam welded to a tantalum tube. The cathode diameter was restricted to 3.2 mm because of dimensional limitation in the discharge chamber. Tests were conducted with cathode orifice diameters ranging from 0.36 to 0.64 mm as suggested by J. D. Sovey.[12]

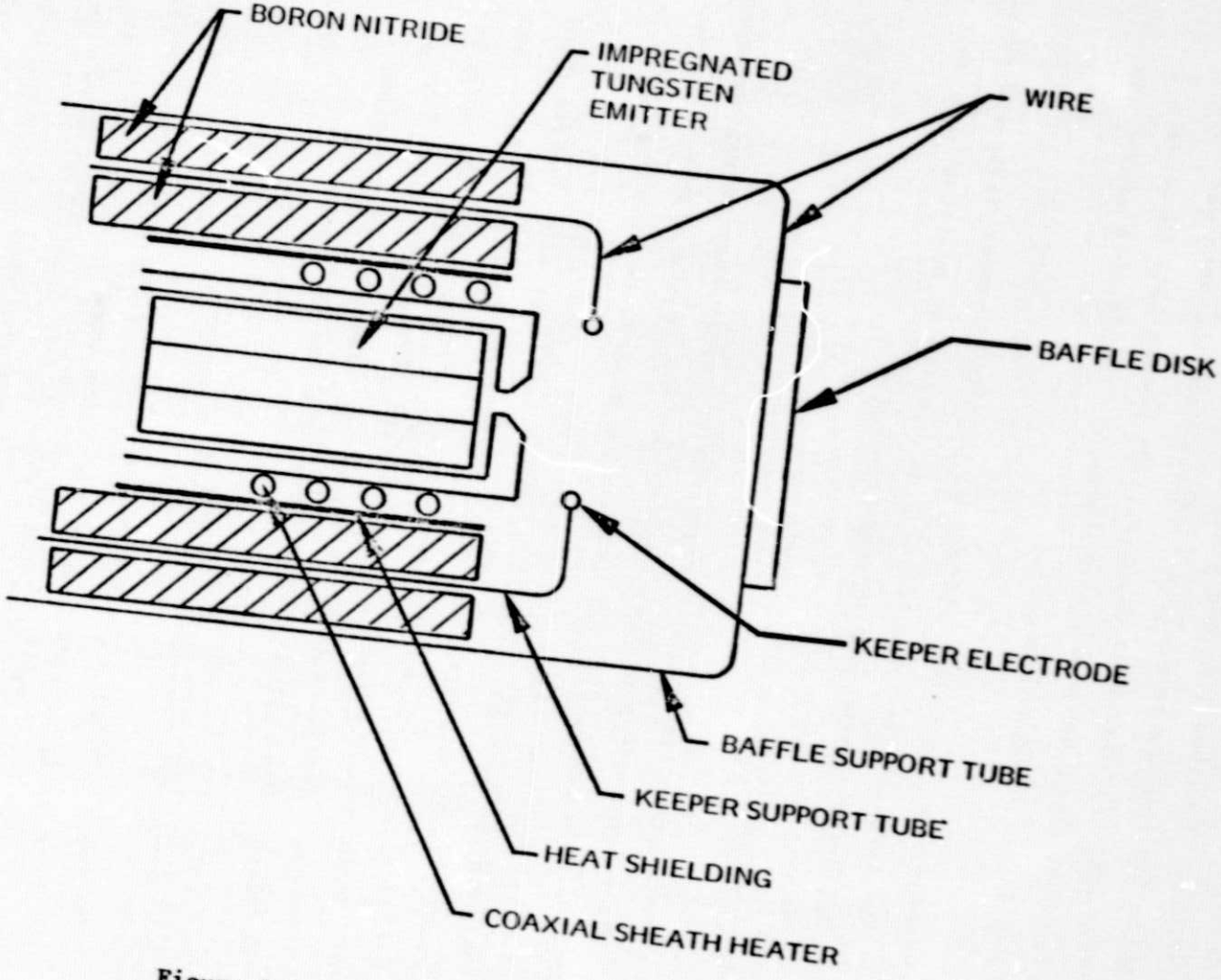

Figure 2-2. Cathode Subassembly

The cathode was heated to temperature with a coil of swaged refractory heater wire slipped over the cathode. The heater sheath was 1.0 mm diameter with a 0.25 mm diamater tungsten rhenium conductor. This design concentrates the cathode energy into the emitter. Electrical continuity was established by crimping the sheath to the conductor at the downstream end of the element.

A barium aluminate impregnated porous tungsten emitter was used in testing. Its dimensions were 2.54 cm long by 0.24 cm outside diameter and 0.114 cm inside diameter as suggested by W. Kerslake.[11] Tests were conducted with the emitters located against the upstream surface of the orifice plate.

The cathode orifice plate was located 1.0 to 1.5 mm upstream of the discharge chamber axial magnetic field maxima. In the original MESC development effort report by Moore,[7] it was found that electron injection at 1.3 mm upstream of the maxima minimized discharge plasma impedance and/or the cathode flow needed to achieve it. Moving the cathode further upstream increased the impedance and produced discharge oscillations. Downstream movement increased the discharge energy or eV/ion. These results were reconfirmed in inert gas ion source optimization tests.

2.1.2.2 Cathode Subassembly

The keeper electrode was 3.2 mm diameter ring of 1.0 mm tantalum wire suspended 1.5 mm from the face of the cathode. The ring was held in position with four tantalum wires spotwelded to a stainless steel keeper tube. The keeper was positioned by tube movement. Boron nitride sleeves electrically isolated keeper potential hardware from the cathode heat shielding and the baffle tube.

A control rod through the vacuum bulkhead positioned the 1.6 mm diameter baffle support tube on the ion source centerline. The baffle disk was cantilevered on the end of the housing tube with spotwelded stainless wires.

2.1.3 PRELIMINARY CATHODE TEST

Preliminary cathode tests were conducted to investigate certain aspects of cathode design. The tests evaluated operational effect of changes in the heat shielding, keeper electrical isolation configuration, and cathode orifice size.

Tests were conducted in a 30 by 90 cm stainless steel vacuum system pumped by a 25 cm diameter oil diffusion pump equiped with a freon-chilled cyro elbow. The relative limited pumping speed for a noncondensible gas restricted the tests to gas flows less than 700 mA equivalent. Calibrated power conditioner meters and a rotometer measured the electrical characteristics and cathode gas flow rate.

A 29 mm diameter cylindrical anode with a stainless steel screen over the downstream end was used in testing. The screen had a geometric transparency of 30 percent. The screen open area plus the area between the baffle housing and anode was equal to about 1/3 the open area of the accel grid used in the ion source tests. The test apparatus is shown in figure 2-3.

2.1.3.1 Component Tests

Different heat shielding configurations were tested to determine which provided the minimum operational temperature and maximum thermal isolation between the cathode and ion source pole magnet. The best results were seen with three layers of 1 mm thick fiberfrax paper, 2.0 cm long, set back 0.6 cm from the cathode orifice plate. Further reductions in the shielding dimensions increased the cathode pole magnet temperature above 210°C reducing the magnetic field.

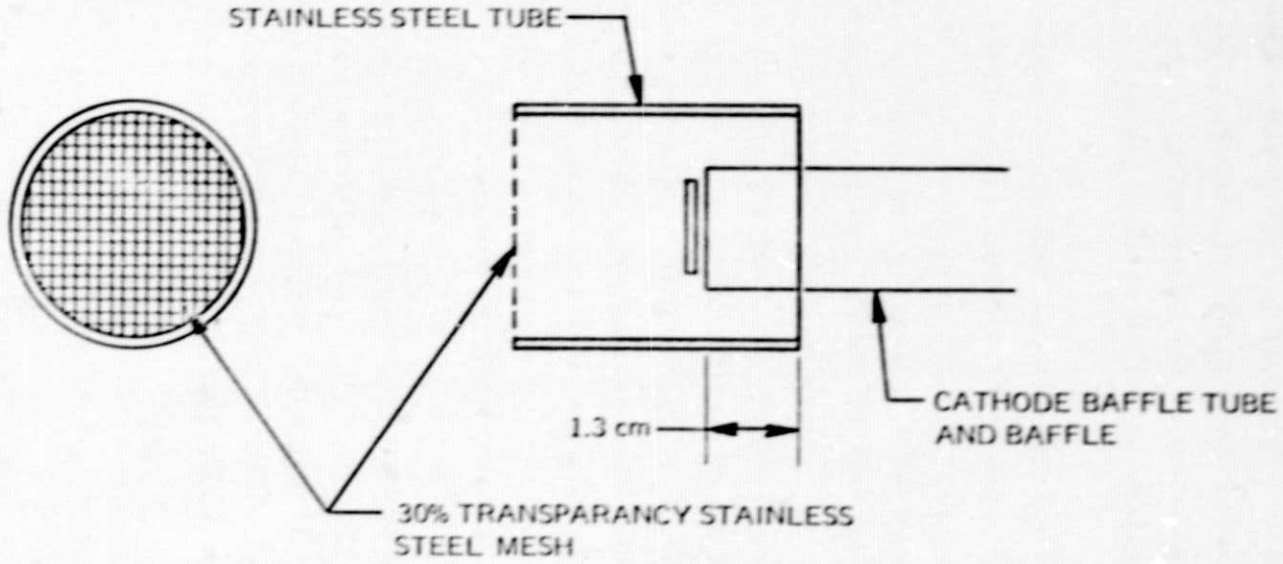

Figure 2-3. Cathode Test Apparatus

The keeper electrode was used to initiate and maintain the discharge. J. D. Sovey[12] found inert gas discharge initiation could be enhanced by applying a 3.0 kilovolt pulse to the keeper during startup. The cathode subassembly used in MESC inert gas tests was originally designed for mercury operation where a 300 volt dc potential was applied to initiate the discharge. Use of the pulse starting technique required improvement of the electrical isolation between the keeper and cathode.

Test results found boron nitride sleeves between the keeper and the baffle housing tube and cathode could stand off the pulse potential. The sleeves initially were plagued with electrical breakdown across the downstream edge after several hours of operation. Reducing the length of the sleeves positioned the face 1.3 cm upstream of the orifice plate eliminating the problem.

Different cathode orifice diameters were tested to determine the correlation between orifice size and orifice plate temperature during spot mode operation. A 1.5 mm thick by 3.2 mm diameter thoriated tungsten orifice plate was used. For these tests, the orifices were countersunk 0.75 mm on the downstream surface and ranged from 0.33 to 0.58 mm in diameter. Orifice plate temperature was measured with a 3 power optical pyrometer through a view port located 60 cm downstream of the cathode.

Test data showed cathode operational temperatures were a function of emission current and/or orifice diameters. Temperatures were found to be directly proportional to emission currents for cathodes with the same orifice diameters. Conversely, the fourth power of temperature was found to be inversely proportional to orifice area for cathodes with differing orifice diameters when operated at similar emission currents. More concisely,

$T \sim A\, I_e$ where I_e = cathode electron emission current

Using the Stefan-Boltzman relationship:

$$\frac{d_1^2}{d_2^2} = \frac{\epsilon_2 \sigma T_2^4}{\epsilon_1 \sigma T_1^4} \quad \text{at fixed } I_e$$

Where $\epsilon_1 \neq \epsilon_2$ as emissivity was a function of temperature.[14] The temperature ratios at different electron emission currents shown in table 2-1 were take from tests conducted with 0.33 and 0.43 mm diameter orifices h the same heat shielding and keeper electrode configuration.

TABLE 2-1

CATHODE ELECTRON EMISSION CURRENT VERSUS RADIATIVE ENERGY LOSS

Electron Emission Current (Amps)	$\frac{d_1^2}{d_2^2}$	$\frac{\epsilon_2}{\epsilon_1}$	$\frac{T_2^4}{T_1^4}$	$\frac{\epsilon_2 \sigma T_2^4}{\epsilon_1 \sigma T_1^4}$
0.70	0.58	0.9	0.67	0.61
1.10		0.88	0.72	0.63
1.50		0.84	0.85	0.71
2.20		0.82	0.74	0.61

Where:

d_1 = 0.33 mm

d_2 = 0.43 mm

T_1 = Temp 0.33 mm orifice

T_2 = Temp 0.43 mm orifice

ϵ_1 = Emissivity of 0.33 mm orifice

ϵ_2 = Emissivity of 0.43 mm orifice

Columns number 2 and 5 show fairly good experimental agreement. Cathode temperature versus electron emission current characteristics were found to change with time and emission current operational level.

Initial "darkening" was quite rapid with the rate of change in apparent emissivity diminishing with time. Changes in emissivity were approximately exponential and could be represented by the class of functions:

$$\epsilon = \epsilon_o + \Delta\epsilon = \epsilon + \epsilon' \ (1 - e^{-t/k})$$

Where:

ϵ = emissivity

ϵ_o = original emissivity

ϵ' = emissivity change characteristic of material

k = a constant determined from emission current operational level

t = time, (duration of operation)

Table 2-2 shows cathode operational test results.

The cathode temperature-versus-electron emission current linear relationship was later applied to operation of a cathode in the ion source. Using a curve produced from the 0.43 mm diameter cathode data shown in table 2-2, the temperature of a 0.58 mm diameter cathode operating at 2.7 amperes of emission* was calculated to be 1369°C. Measurement of the cathode temperature with a platimun-platimum rhodium thermocouple found it to be 1290°C or about 6 percent in error. This represents fairly good agreement, as the calculated temperature was based on extrapolating the 0.43 mm cathc e orifice data at 2.2 to 2.7 amps operation and no correction was made for the time-history emissivity changes. Comparison of calculated and test cathode temperatures are presented in table 2-3.

---

*Ion source cathode electron emission current was defined as:

$$\text{Emission current} = J_E - J_1 + J_A$$

where J_E is the discharge current, J_1 the positive high voltage supply current and J_A the negative high voltage supply current.

TABLE 2-2

CATHODE OPERATIONAL TESTS RESULTS

24 May 77
Tests conducted with 0.33 mm diameter orifice. Lapsed time increases going down the column.

ΔV_1 (volt)	J_E (amps)	V_{CK} (volt)	J_{CK} (amps)	T_C (°C)	Mass Equiv Flow (amps)	Chamber Pressure (torr)
31.3	.70	21.4	.400	1172	.634	1.1×10^{-4}
30.0	2.20	15.3	.400	1350	"	"
29.3	1.50	16.0	.410	1250	"	"
29.7	1.10	18.0	.400	1190	"	"
31.3	1.10	19.0	.400	1188	.329	5.5×10^{-5}
30.3	1.50	16.5	.400	1230	"	
51.2	1.50	18.7	.400	1227	.220	3.5×10^{-5}
51.2	1.10	21.8	.400	1179	"	"

25 May 77
Tests conducted with a 0.43 mm diameter orifice. Lapsed time increases going down the column.

30.8	1.10	18.4	.400	1147	.507	8.0×10^{-5}
30.5	1.10	18.0	.400	1130	.507	8.4×10^{-5}
30.1	1.10	17.8	.400	1135	"	"
29.3	1.53	15.6	.402	1200	"	"
28.7	1.52	15.0	.402	1181	.645	1.2×10^{-4}
27.4	2.22	12.7	.400	1250	"	"
29.1	1.10	17.0	.400	1130	"	"
33.0	1.10	18.7	.400	1135	.318	5.6×10^{-5}
32.1	1.50	16.7	.400	1200	"	"
39.5	1.45	18.4	.400	1203	.220	3.5×10^{-5}
40.3	1.10	20.5	.400	1130	"	"

TABLE 2-3

CATHODE TEMPERATURE CALCULATION FOR 0.58 mm ORIFICE

Cathode Electron Emission Current (Amp)	Calculated Cathode Temperature (^{o}C)	Measured Catode Temperature (^{o}C)	% Error (%)
2.75	1219	1130	8
2.90	1233	1150	7
3.15	1256	1180	6
3.75	1339	1280	5

2.1.3.2 Cathode Test Conclusions

The above discussion correlated changes in cathode-to-cathode operational temperatures to orifice area differences by empirical use of the Stefan-Boltzmann radiative energy formula. Agreement between calculated and measured temperature of cathodes operating at the same emission current with different orifice sizes implied radiative energy losses from the emitter cavity governed operational temperatures, or the cathode functioned as a classic blackbody. Further, the operational temperature of any particular cathode orifice size was found to be a function of cathode electron emission current and independent of keeper and main discharge power. This indicated cathode temperature was controlled by the electron emission mechanisms; thus emitter design could possibly be utilized to reduce cathode operational temperatures.

It must be pointed out the cathode temperature-orifice area relationship was based upon the results of a few tests and should not be viewed as conclusive. Further testing in this area was beyond the scope of this program.

2.1.4 ELECTRODE DESIGN

Recent papers from LeRC, HRL, and the University of Colorado[13] have reported thruster performance improvements due to the use of a Small Hole Accelerator Grid (SHAG) design. Two different methods have been used to fabricate SHAG optics. Either allow the individual ion beamlets to bore (ion machine) the accel grid hole pattern in a blank piece of molybdenum or predrill the grid to approximately 20 percent transparency. The second method was used as it required less non-optimal ion source testing time.

The screen electrode design had 2269 holes 2.236 mm diameter located on 2.54 mm centers. This pattern produced a 70 percent transparent electrode. The accel had 1.17 mm diameter holes in the same pattern producing a grid with 20 percent transparency. The accel-to-screen hole positions were not compensated to minimize beam spread. Both grids were made from 0.38 mm thick molybdenum that were hydroformed with a 5.0 mm dish. The electrodes were mounted on the discharge chamber with the dish curving downstream. Accel-to-screen electrode gap was set at 1.0 mm (cold).

2.2 POWER CONDITIONER

The power conditioner (PC) used in testing the source was originally designed for cesium ion thruster operation. It was built as a semi-flight type breadboard with the high voltage and arc supplies controlled through dc input to a 20 kHz inverter. Heater power was provided by autotransformers and isolation transformers. Figure 2-4 shows a schematic layout of the power conditioner. Converting the PC to inert gas operation necessitated some rework because of the increased power requirements. This included increases in the ion beam current capability and arc power and the addition of a keeper supply.

61150

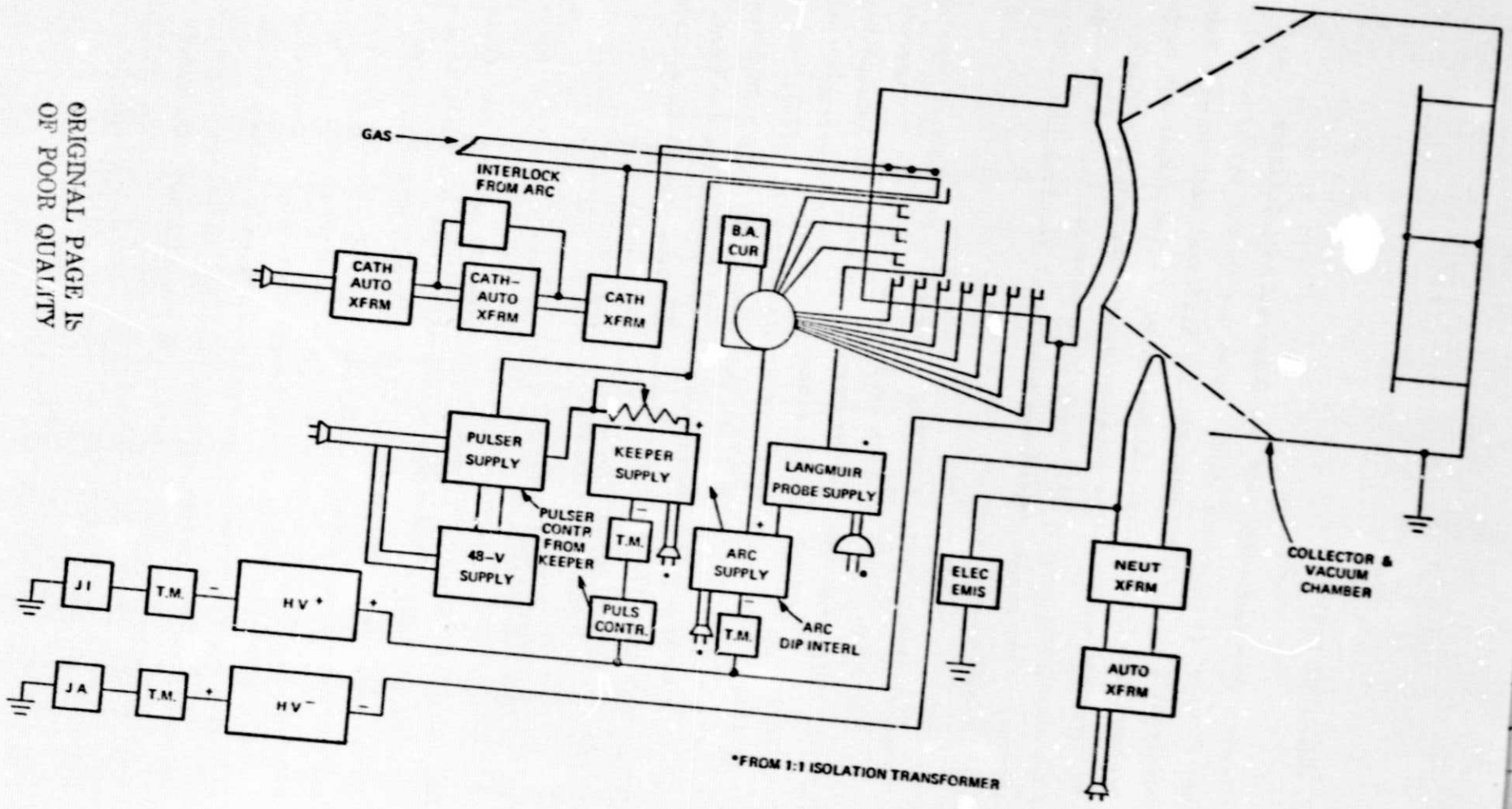

Figure 2-4. Power Conditioner Schematic

2.2.1 ARC AND KEEPER SUPPLIES

A design study conducted early in the program found it was more cost effective to use electrically isolated dc laboratory supplies to control the arc and keeper than modify the power conditioner. Several suitable dc supplies and isolation transformer were available from the XEOS equipment pool. Modifications for inert gas arc and keeper supplies were a matter of physically removing the existing components and installing the laboratory supplies. Provisions were made to insure the laboratory supplies would be compatible with source operation. These included an "arc-dip" circuit and keeper transfer circuit.

The arc-dip circuit decreases the arc voltage in the event of a high voltage supply overload. This action reduces the discharge plasma extrusion in the interelectrode gap and aids in reestablishing source operation. Once the overload disappears, the arc voltage is brought up nominal operating level over a period of 0.5 to 1.0 second.

Keeper control circuitry supplies a high voltage pulse to the electrode when no keeper discharge is present. The 2 to 3 kilovolt pulse circuit was supplied GFE from LeRC. It was wired in series with the dc laboratory supply as long as the keeper discharge was less than 2.0 milliamps. Once the discharge initiated, the pulser was electronically removed from the circuit and the dc supply used to sustain operation.

2.2.2 HIGH VOLTAGE POWER SUPPLIES

Electrode perveance is a function of the inverse square root of the ionic atomic mass. The small atomic mass of argon made it necessary to increase the positive high voltage supply current/power capability. This was accomplished by adding 50 percent more inverter drive.

The original transformer was overdesigned by a factor of 175 to 200 percent. This allowed the drive to be increased without the danger of core saturation. The additional drive allowed the positive high voltage overcurrent trip point to be raised from 0.600 to 0.900 ampere. During source testing, this was found to be insufficient to attain maximum steady state beam possible at a 1000 volt extraction potential. Program time and resource limitation prevented further high voltage supply modification.

2.3 TEST INSTRUMENTATION AND MEASUREMENTS

To evaluate discharge chamber performance it is necessary to know the discharge power, ion beam current, ion beam distribution and mass utilization efficiency. The latter is determined from propellant flow rate, ion beam current, state of ionization and the backstreaming neutrals flow from the vacuum chamber through the grids. The backstreaming neutral flow was calculated.[15] The other parameters were measured.

2.3.1 TIME-OF-FLIGHT COLLECTOR

Time-of-flight (TOF) data were collected to find the percentage of single and double charged ions present in the beam as a function of applied anode potential. Ions extracted from the discharge plasma acquire an exhaust velocity proportional to $e^{1/2}$, where e is the ionic charge. Switching off the extraction voltage interrupts the ion current from the nominally operating discharge plasma. After interruption, a beam collector time-current profile shows two current levels as a function of time reflecting the different ionic velocities. The current level differences are used as a measurement to determine relative percentage of single and double charged ions.

The 60 cm diameter stainless steel time-of-flight collector was 3.0 meters from the face of the accel grid. RFI shielding was provided by a ground potential collector housing with two electrically isolated

tungsten wire grids. The grids were positioned between the beam plasma and collector. The upstream and downstream grids operated at ground and negative 40 volts respectively, to minimize collector signal noise and suppress secondary electrons. The collector operated at ground through a 100 ohm resistor.

The double charged ion current in the exhaust beam was measured by instantaneously grounding the positive high voltage supply output and measuring the collector current as a function of time. Collector current-versus-time characteristics were measured by monitoring the potential across a resistor in the collector lead with an oscilloscope. The scope was triggered by a transient from the high voltage grounding apparatus as shown in figure 2-5 and recorded with a camera. Several traces were photographed at each discharge potential.

The scope was used in a single sweep mode with a selected sweep rate of 50 microseconds/cm. A one-to-one probe was used with a y-axis scale of 0.2 volts/cm. Times necessary to travel the 3.0 meters were computed using the kinetic energy relationship.

$$t = \frac{d}{\sqrt{\frac{2\,e\,V}{M}}}$$

Where V was the applied extraction potential and M the atomic mass.

Calculations found a 1000 volt argon beam took 43 and 30 microseconds, respectively, for the single and double charged ions to traverse collector-to-source distance. Single and double charged xenon ions arrived at the collector 86.5 and 50 microseconds, respectively, after beam interruption. At 50 microseconds/cm sweep, the single and double charged argon ions currents were separated by 2.6 mm and single and double charged xenon currents by 4.7 mm.

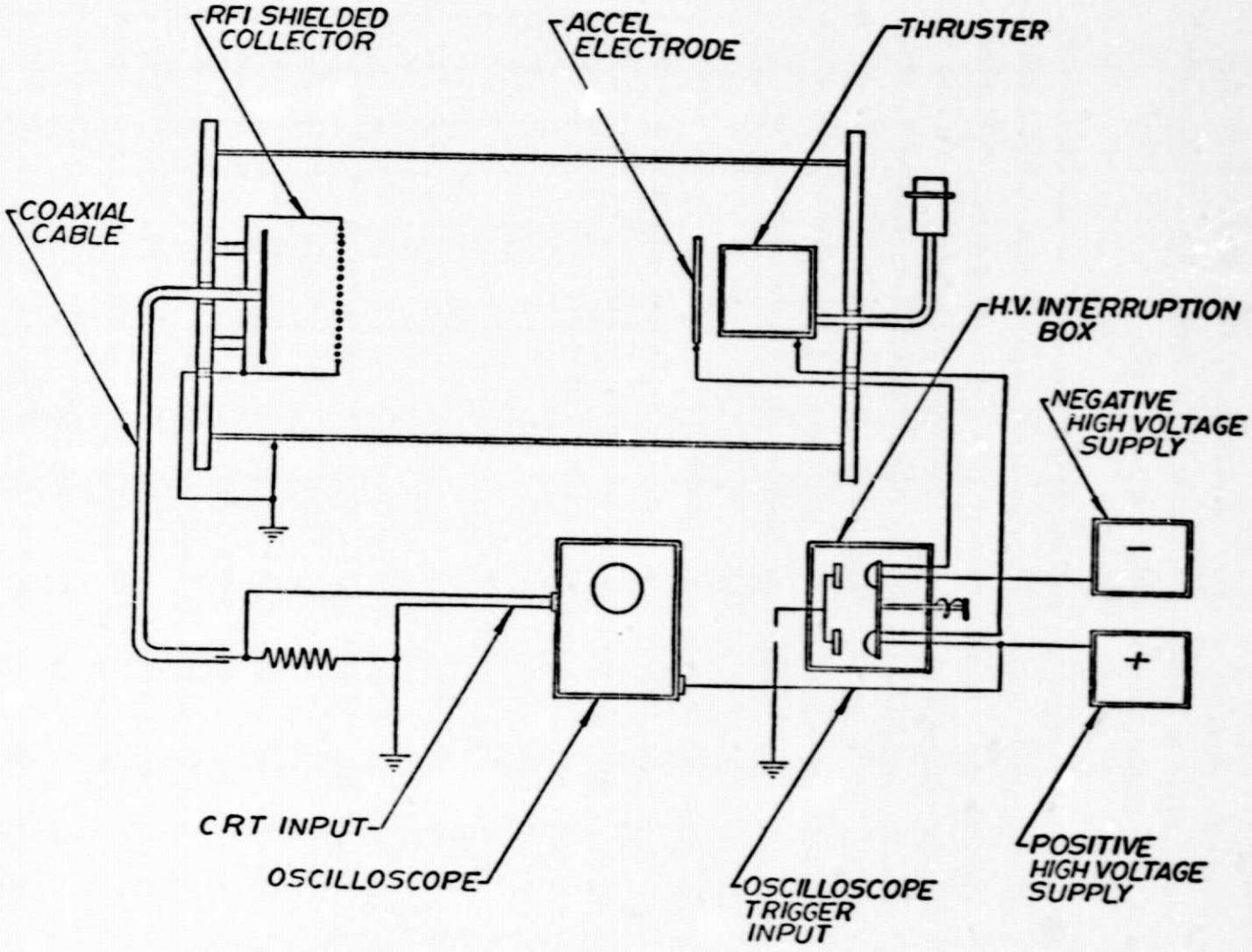

Figure 2-5. Time-of-Flight Apparatus

Faster sweep rates were precluded by the one-to-two cycle overcurrent response of the 20 kHz inverted high voltage supply and the stored charged in the system. Stored charge was due to system filtering that added several RC time constants, and produced a 142 microsecond current "roll off" in the current-versus-time collector profile. When the time constants added together, the collector current took as long as 320 microseconds to go to zero after the removal of high voltage. The 50 microseconds/cm sweep rate allowed the entire beam decay to be displayed while still providing adequate resolution to identify the singly charged ion current plateau.

2.3.2 FARADAY BEAM PROBE

Three Faraday cup type probes were used to measure the ion beam distribution by traversing through the beam plasma at right angles to the thruster centerline. Two probes crossed the beam axis 22 cm downstream of the accel while a third crossed at 30 cm as shown in figure 2-6. One of the two at 22 cm was a slit probe. The other two were cylindrical probes with a 1.27 cm orifice. Slit probe data were used to measure beamspread and to confirm the cylindrical probe was collecting the entire beam width. During operation the probe collectors were biased negative with respect to ground to minimize electron collection. No electron surpression grids were used on the probes.

The slit probe was a tube-in-a-tube assembly with the 1.27 cm diameter internal tube used as the probe collector. Electrical isolation between the tubes was accomplished by short teflon sleeves on the ends of the internal tube. The collector tube had a 25.5 x 0.64 cm opening that was aligned with the opening in the outer tube. (The tubes had wall thicknesses of 0.38 mm.)

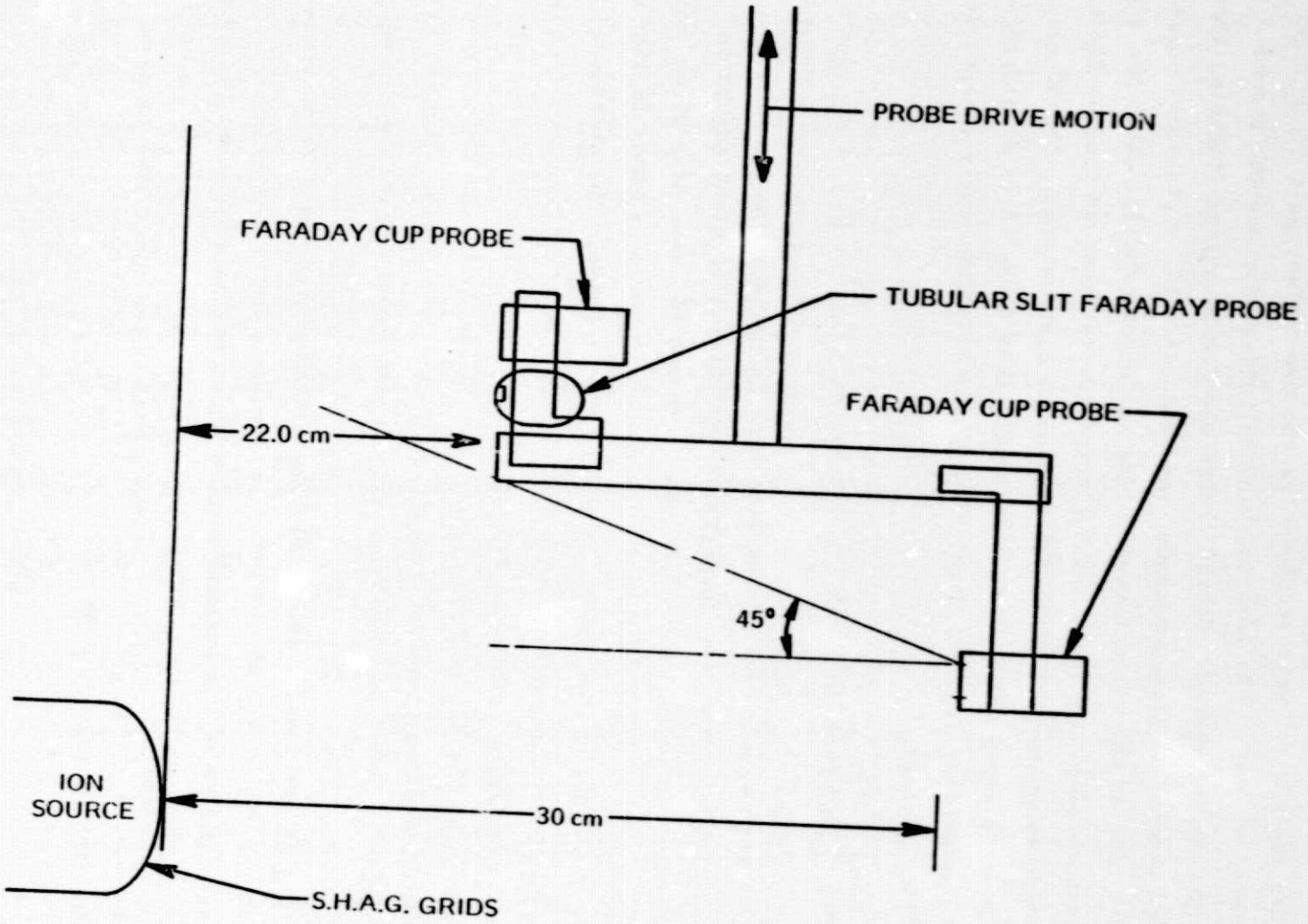

Figure 2-6. Faraday Cup Probe Drive

Data from the three probes were recorded on an x-y plotter with the x-axis indicating probe drive position and the y-axis recording the beam current collector by measuring the potential across a 300 ohm resistor.

The 25.5 cm wide slit allowed accurate location of the beam envelope edge with up to 30 degree horizontal misalignment between it and the probe center line. The dimensions above produced a slit probe vertical acceptance angle of:

$$\alpha = \tan^{-1} \frac{\frac{0.64}{2} + \frac{0.44}{2}}{2\ (0.38) + .32 + 1.64 \cos \tan^{-1} 0.64} = 28 \text{ degrees}$$

The cylindrical probes were 2.5 cm in diameter with 1.27 cm orifices and 1.9 cm stainless steel disk collectors. The 0.05 cm thick orifices were located 2.16 cm from the collectors producing an acceptance angle of:

$$\alpha = \tan^{-1} \frac{\frac{1.9}{2} + \frac{1.27}{2}}{2.16 + 0.05} = 36 \text{ degrees}$$

2.3.3 LANGMUIR DISCHARGE PROBE

A 2.0 mm by 0.46 mm diameter sheathed heater type Langmuir probe was used to measure discharge chamber plasma characteristics. The probe was attached to a vacuum bulkhead control rod for positioning. Rod motion located the probe 1.22 to 5.54 cm from the discharge chamber center line in the plane of boundary anodes 2 through 5. A schematic numbering the boundary anodes is shown in figure 2-7.

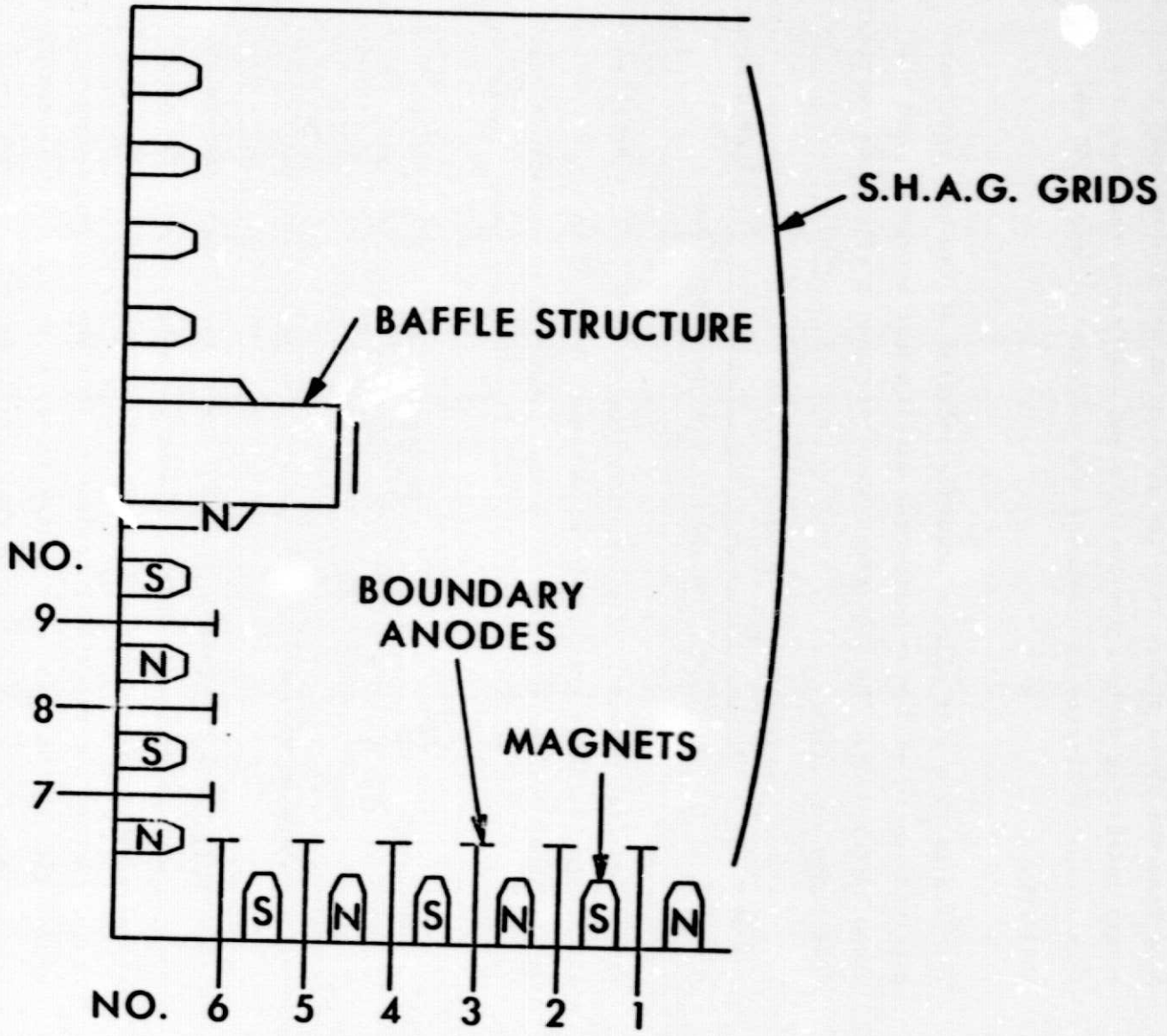

Figure 2-7. Cutaway Schematic 12 cm MESC Discharge Chamber

Photographs of the discharge chamber and probe are shown in figures 2-8 and 2-9. The former shows the probe in the plane of boundary anode number 5 located 1.22 cm from the discharge chamber center line. The second photograph shows the probe in the plane of boundary anode number 2 positioned 5.54 cm from the discharge chamber center line. The 5.54 cm position was directly upstream of the outermost hole in the extraction grids.

An anode potential dc power supply was used to collect Langmuir probe data. An isolation transformer in the ac line prevented electrical breakdown between the output and chassis as the entire supply was biased to positive high voltage plus the arc potentials. Lucite control rods were used to change the supply potential and protect the operator from high voltage. Probe data were collected by manually changing the supply output potential and recording voltage and current at selected positions in the discharge plasma. Plasma measurements were made at potentials positive and negative of the anode reference.

2.3.4 FEED SYSTEM

The feed system design was a simple array of valves, flow meters and gas bottles (figure 2-10). Gross gas flow measurements were taken from rotometers in the cathode and main feed lines. More accurate measurements were made by running the input gas through a precision mass flow transducer. The rotometers were capable of measuring gas flow to an accuracy of $\pm$0.21 ml/minute under ideal conditions. By comparison, the XEOS supplied Hastings-Raydist mass flow transducer had an accuracy of $\pm$0.1 ml/minute with up to 20 percent variation in temperature and/or pressure. The transducer resolution was equivalent to being able to measure the gas flow to within $\pm$10 mA. Two-stage needle

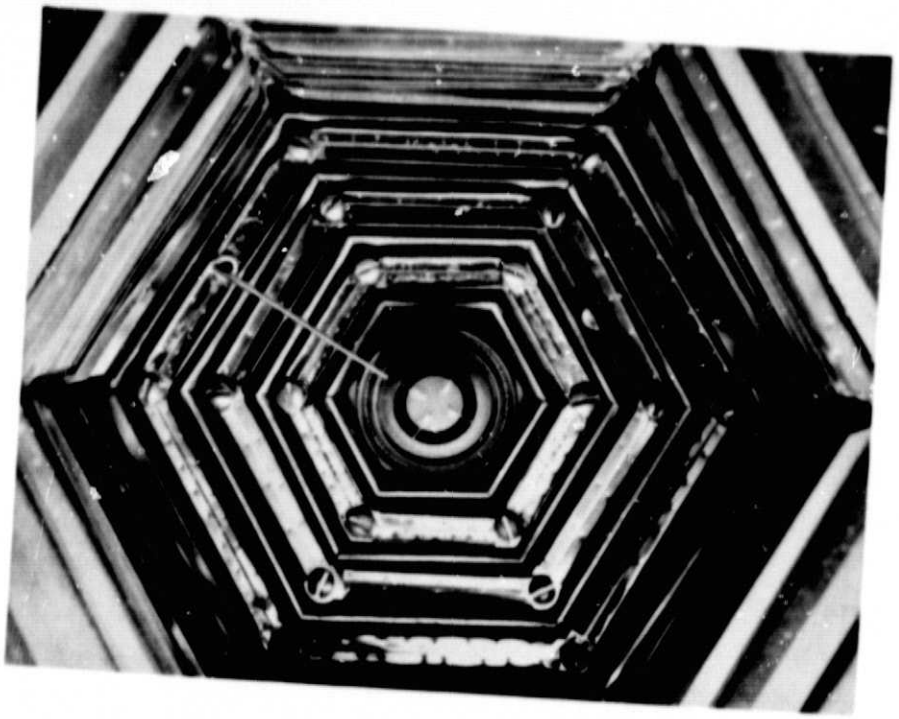

Figure 2-8. Langmuir Probe 1.22 cm from Discharge Chamber Centerline

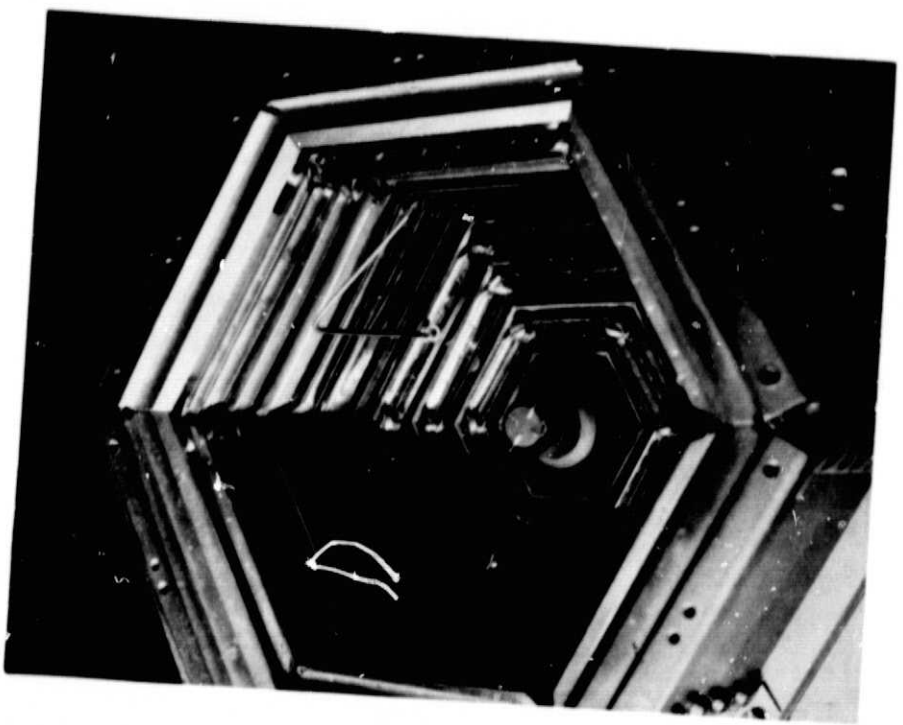

007767

Figure 2-9. Langmuir Probe 5.54 cm from Discharge Chamber Centerline

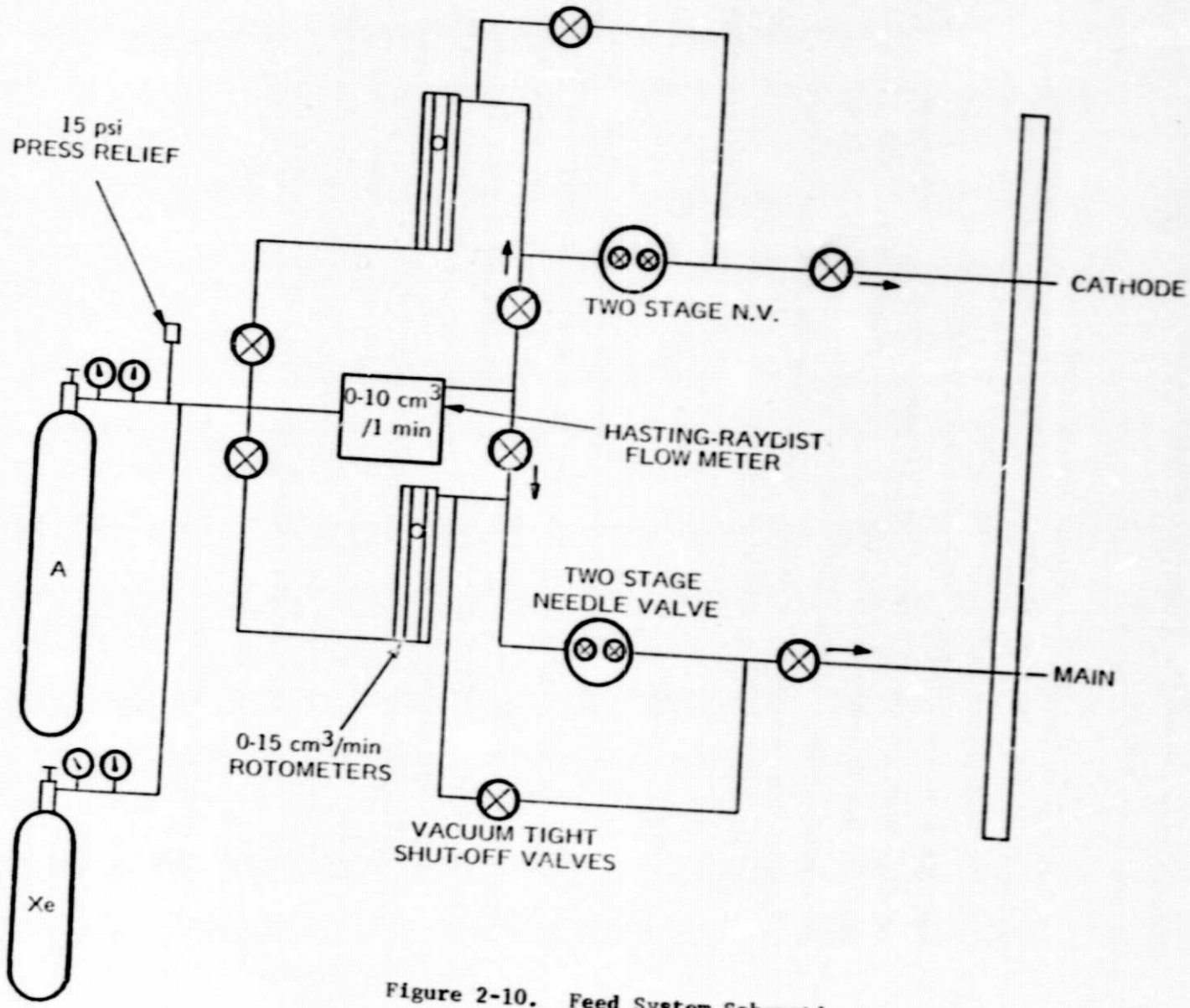

Figure 2-10. Feed System Schematic

valves controlled gas flow to the main feed ring and cathode. The pressure drop across the rotometer and transducer are negligible at the gas flows tested.

The feed system operated at vacuum system ground potential. Source feed system electrical isolation was achieved by including two meters of 0.625 cm diameter teflon tubing between the vacuum flange and the downstream shut-off valve. The valve was electrically tied to the vacuum system ground to insure test personnel safety. System overpressure was prevented by placing a 15 psi pressure relief valve between the output of the regulators and the feed system plumbing. A pumpout line shunted the needle valves to allow thorough evacuation of the plumbing prior to changing gases.

2.4 VACUUM SYSTEM

Tests were conducted in a 1.5 m diameter by 4 m long horizontal vacuum chamber. Pumping was provided by six 25 cm diffusion pumps. At the start of the program, an argon pumping speed test was conducted with no discharge chamber (see table 2-4). The minimum chamber pressure with no propellant gas flow was 1.0×10^{-7} torr. Flow rates up to 626 milliamperes equivalent could be accommodated by the pumps at chamber pressures less than 2.0×10^{-5} torr. The measured pumping speed per pump is 1000 liters/second which is 1/4 of the 4000 liters/second manufacturer's specification. Most of the pumping speed loss is due to cyro elbow impedances which are in series with each pump. No pumping speed differences were seen between the cyro elbows chilled with freon and those chilled with LN_2.

TABLE 2-4

FACILITY PUMPDOWN TEST RESULTS

Vacuum Chamber Pressure (Torr)	Anode Flow (mA/Equiv.)	Cathode Flow (mA/Fquiv.)	Total Flow mA/Equip.)
5.3×10^{-5}	748	935	1684
3.8×10^{-5}	973.6	290	1263
2.6×10^{-5}	627	295	922
2.0×10^{-5}	415	211	626
1.0×10^{-5}	331	46	377
8.2×10^{-6}	267	47	314
6.3×10^{-6}	141	71	212
8.2×10^{-6}		297	297
6.2×10^{-6}			234
4.0×10^{-6}		125	125
8.2×10^{-6}	321		321
6.2×10^{-6}	243		243
4.0×10^{-6}	124		124

SECTION 3

RESULTS AND DISCUSSION

3.1 PRELIMINARY TEST RESULTS

3.1.1 POWER CONDITIONER CALIBRATION TESTS

Power conditioner calibration tests were conducted to ensure test data reliability. Calibration consisted of correlating power conditioner panel meter readings with those of precision meters with known NBS calibration curves. This was accomplished by simultaneously recording the current and voltage to a test load from both sets of meters. The results were plotted as precision versus panel meter readings for the power conditioner voltmeters and ammeters.

Panel meter readings were typically with 2 percent of the NBS values with no evidence of hysteresis. All panel meter characteristics appeared to be linear.

The calibration curves produced by these tests were used in the reduction of test data. Panel meter readings were recorded on data sheets during ion source tests.

3.1.2 FLOW METER CALIBRATION TESTS

To find the mass utilization it is necessary to know the ion beam current, ionization state of the beam ions, the backstreaming neutrals propellent atoms from the vacuum system, and the amount of propellant gas fed into the discharge through the anode feed ring and cathode. Beam ionization state is determined by measuring the properties of the extracted beam. Backstreaming neutrals flux into the discharge chamber

can be calculated from the background pressure and kinetic theory of gas. Discharge chamber inlet gas flows are measured with gas flowmeters.

As the inlet flow rates dominated mass utilization efficiency calculations, the accuracy of those calculations depended upon the accuracy with which the gas flow measurements are made. Flow meter calibrations ensure the validity of these instrument readings.

The rotometers and transducer were calibrated by measuring the volume of water displaced by a constant flow of gas as a function of time. For these measurements, a water filled graduated cylinder was inverted in a beaker of distilled water. Each test was started after it had been established the gas flow rate into the tube was constant with time.

Tests were conducted at six different flow rates with argon. Xenon flowmeter calibration was calculated from the argon data. These flows ranged from 0.5 to 11 milliliters/minute (ml/min) with a minimum displaced volume of 20 milliliters at the lower flow rates. Two tests were conducted for each flow rate

Data were reduced by correcting for the increase in pressure due to the decrease in water height in the graduated cylinder and dividing the corrected volume by the time required to displace it. The computed results were compared with the manufacturer's supplied calibration curve.

Good agreement was found between the computed results and the manufacturer's data for the Hastings-Raydist mass flow transducer. Rotometer readings were found to vary as much as 3 percent from test to test and deviate up to a maximum of 38 percent from the curves supplied with the instruments. Test-to-test variation can be attributed to static charge build up on the sapphire ball "float" causing it to

adhere to the tapered glass bore of the rotometer. The rotometer deviation from the manufacturer's supplied curve converged with the experimental one at flows greater than ~ 6 ml/min. The rotometers were used primarily to adjust the cathode and main feed flow rates. Ion source mass utilization efficiency was calculated from transducer mass flow data. The exception of this procedure occurred during "mixed mode" ion source operation. In this situation, different gases were fed into the discharge through the cathode and the main feed. Mass utilization efficiency was calculated using the transducer data for cathode flow and rotometer data for the main feed. These calculations should have an error of less than 3 percent as the rotometer data were corrected with the calibration curve for the main feed.

3.1.3 NEUTRALIZER TESTS

Preliminary ion source tests were conducted with a tantalum filament neutralizer immersed in the ion beam plasma. The wire was 0.25 mm diameter and 75 mm long and was mounted on alumina pillars 0.64 cm downstream of the ground screen surface. Filament power was supplied from the isolation transformer and auto-transformer shown in figure 2-3. Neutralizer tests were discontinued after it was established no differences existed in test results obtained during filament "on" or "off" operation. No emission current was seen during any test.

3.2 SOURCE PERFORMANCE MAPPING AND OPTIMIZATION

3.2.1 TEST PHILOSOPHY

Ion source optimization was accomplished by varying source operational parameters in a systematic manner. Data from each test were reviewed and the extracted information used to improve source performance by reconfiguring the interacting components in the MESC

design discharge chamber. These are, in order of impact on performance: boundary anode position, cathode baffle and baffle tube location, and cathode structure.

The boundary anode array serves two purposes. For a particular arc voltage, the anodes must be set at the right position in the boundary magnetic field to minimize ionic recombination losses on the pole faces, but still collect enough electron current to sustain the discharge without producing ion source inefficiency. For optimal performance, the arc potential must be the minimum necessary to maximize primary electron ionization probability. Experience has found this potential usually to be approximately three or more times the first ionization potential.

Mapping thruster operation to determine where the boundary anodes are in relation to their optimal position involves changing the arc voltage at several different cathode/anode mass flow ratios and extraction voltages.

Ion source tests usually followed the same rough outline, with data recorded between each operational parameter change. Once the gas flow rate was confirmed to be stable at a convenient level, the baffle assembly was adjusted for maximum arc current. Next, the arc potential was varied in a step-wise manner from the lowest stable potential to at least 10 volts above the operational nominal. If mass utilization efficiency was promising and the are impedance 12 to 16 ohms, further data were collected. If not, the cathode/main gas flow ratio was changed and the procedure repeated. Measurements were repeated at least three times at three different total mass flows for each boundary anode and baffle configuration and gas tested.

Rapid feed system gas changeover capability made it possible to test boundary anode and baffle configurations with argon and xenon during the same system pumpdown. This procedure minimized the time required to test each configuration.

3.2.2 ARGON OPERATION

Argon mass utilization efficiency of 75 percent, corrected, was achieved at 351 eV/ion (see table 3-1). The exhaust ion beam ($J^+ - J^-$) was corrected by subtracting one-half the double charged ion current and the total calculated flux of backstreaming neutrals[15]. This type of ionic bookkeeping counts the double charged ion as one ion by accounting for the factor of two difference in its charge-to-mass ratio.

TABLE 3-1

ARGON OPERATION

D.P.	H. V.* (Volts)	J^+ (Amps)	H.V.* (Volts)	J^- (Amps)	Arc		Keeper		Cathode Mass Equiv. (Amps)	Total Mass Equiv. (Amps)	eV* Ion	eV** Ion	% Double Charged	Mass*** Eff. (%)
					Voltage (Volts)	Current (Amps)	Voltage (Volts)	Current (Amps)						
Chamber Pressure 3.8 x 10^{-5} torr - Backstreaming Neutral Ingestion 0.030 amp Equivalent														
1159	1100	.742	400	.011	47	4.20	8.2	0.25	.374	.984	272.	279.	4.6	67.8
	1200	.760		.011	47	4.50	8.0	0.25			285.	287.	4.6	69.6
		.780		.011	50	5.00	8.0	0.25			327.	336.	5.3	70.9
		.800		.014	52	5.50	7.0	0.25			366.	376.	5.6	72.6
		.800		.014	56	6.00	7.0	0.25			429.	444.	6.5	71.6
		.710		.011	45	3.00	9.0	0.25			196.	200.	4.0	65.1
Chamber Pressure 4.0 x 10^{-5} torr - Backstreaming Neutral Ingestion 0.034 amp Equivalent														
1150	1200	.760	380	.012	52	3.6	14.5	0.500	.347	.923	259.	266.	4.8	71.40
		.770		.015	54	4.0	14.5	0.500			295.	303.	5.36	73.64
		.820		.017	60	5.8	12.0	0.500			440.	457.	7.5	76.7
		.740		.011	52	3.7	13.0	0.500			273.	279.	4.8	71.4
Chamber Pressure 4.3 x 10^{-5} torr - Backstreaming Neutral Ingestion 0.037 amp Equivalent														
1600	1200	.760	400	.014	49	4.2	12.5	0.500	.276	.962	284.	290.	4.0	70.54
		.820		.015	55	4.9	10.0	0.500			341.	351.	5.71	74.97
		.760		.014	50	4.10	12.5	0.500			283.	289	4.2	70.38
Chamber Pressure 2.5 x 10^{-5} torr - Backstreaming Neutral Ingestion 0.022 amp														
1140	1000	.685	380	.010	49	4.11	13.0	0.50	.347	.858	308.	316.	5.0	72.17
		.685	380	.010	49	4.11	13.0				309.	316.	5.0	72.12
		.720		.012	55	4.55	13.0				362.	374.	6.2	74.75
		.725		.011	55	4.50	12.0				355.	366.	6.2	75.41
		.750		.011	60	4.91	12.0				406.	421.	7.5	77.01
		.560		.008	45	3.20	13.0				273.	279.	4.0	59.16
		.685		.010	50	4.0	13.0	0.50			317.	325.	5.3	71.88

*Discharge and Keeper Power Uncorrected for Doubly Ionized Beam

**Discharge and Keeper Power Corrected for Doubly Ionized Beam

***Mass Efficiency Corrected for Backstreaming Neutral Atoms

Assuming 100 percent ionization of the backstreaming neutrals errs on the conservative side: thus, it is a worst case estimate. However, the error introduced is second order. The backstreaming neutral flux was calculated from the kinetic theory of gases[15] assuming the vacuum chamber pressure was due to neutrals. The calculated flux times the accelerator electrode open area was taken as the mass flow rate into the discharge chamber from the vacuum system. These calculations were based on the following relationship:

$$\dot{m} = \frac{P \quad A_a \quad e}{(2\ MkT)^{1/2}} \quad \text{amperes equivalent}$$

where P was the vacuum system pressure, A_a the accel grid open area, e electron charge and M the molecular mass of the test gas. The neutral atoms temperature was assumed to be 300°K for these calculations. All performance calculations presented have been corrected using the above methods.

3.2.2.1 Argon Performance Optimization

Argon was used as the basic performance test gas for several reasons. First, argon is more difficult to ionize as it has a smaller ionization cross section and higher ionization potential. Hence, more test time was required to achieve good performance with argon than with xenon. Argon discharge chamber operation had a much greater cathode-to-main gas flow ratio and therefore a wider number of test ratios. Secondly, optimum axial baffle position was found to be sharply defined for argon and very broad for xenon discharge operation. Hence, once the optimum position had been located for argon, no further changes were necessary for xenon operation, however, the reverse was not necessarily the case.

The hexagonal MESC discharge chamber had nine boundary anodes wired in parallel to a single arc supply and metered to allow the current to each to be monitored separately. The anodes were numbered from the screen grid to the rear and from the periphery to the discharge chamber center line. Six anodes were located on the side walls and three on the rear wall. Figure 2-6 shows the numbering system in a cutaway schematic of the discharge chamber.

Optimum source performance was realized by adjusting boundary anode positions so the electron current ratios did not exceed 1.3 to 1, exclusive of anodes 1, 6, and 7. The optimum current density ratios were achieved by adjusting the position of the individual anodes. In the mercury discharge position, the magnetic field B_o, parallel to the discharge chamber centerline at the edges of the anode channels averaged 270 gauss. The best argon performance was seen by changing B_o to a generally lower value by moving the anodes further into the discharge. The average field across anodes 2 through 5 was: 223, 190, 163, and 143 gauss, respectively. B_o was 220 gauss across anodes 8 and 9. Anode-to-anode positional differences were probably necessary to minimize ionic wall recombination losses by maintaining constant plasma vicosity with axial variation in plasma density.

The magnetic field configuration described above implies the existence of an axial discharge plasma density gradient. Using the MESC diffusion current formula mentioned in section 2, the density would have to change from anode-to-anode. Plasma density ratios between anode number 2 and anodes 3, 4, and 5 were calculated as 0.85, 0.73 and 0.64. Langmuir probe measurements, discussed in a later section, tended to support these calculations.

Tests also found the anode current distribution could be controlled by the axial position of the baffle assembly. Baffle movement either way

from optimum reduced the current density differences between the anodes at the expense of mass utilization efficiency. Tests were conducted with baffle disk diameters of 0.95 to 1.25 cm and tube-to-disk gaps ranging from 1.0 to 4.5 mm. The greatest mass utilization efficiency at minimum eV/ion was seen with a 1.11 cm diameter baffle disk located 1.6 mm from the support tube face. The disk was positioned 6.4 mm downstream of the cathode orifice plate.

3.2.3 MIXED MODE OPERATION

Argon-like source performance was observed with xenon cathode flows ranging from 0.015 to 0.040 ampere equivalent. Discharge potentials between 47 to 60 volts were necessary to ionize 65 to 71 percent of the total mass flow with discharge energies of 297 to 346 eV/ion respectively (see table 3-2).

TABLE 3-2

MIXED MODE OPERATION

D.P.	H. V.* (Volts)	J* (Amps)	H.V.* (Volts)	J* (Amps)	Arc		Keeper		Cathode Mass Equiv. (Amps)	Total Mass Equiv. (Amps)	eV/ion*	eV/ion**	% Double Charged	Mass Eff.*** (%)
					Voltage (Volts)	Current (Amps)	Voltage (Volts)	Current (Amps)						
Chamber Pressure 3.7 x 10^{-5} torr - Backstreaming Neutral Ingestion 0.030 amp Equivalent														
1630	1150	.715	380	.010	51	3.85	15.5	0.50	.037	.971	289	297.	5.5	65.47
	1150	.760	380	.011	55	4.10	15.0	0.50			311	321.	6.2	69.19
	1150	.795	380	.014	60	4.20	16.0	0.50			332	346.	7.5	71.20

*Discharge and Keeper Power Uncorrected for Doubly Ionized Beam

**Discharge and Keeper Power Corrected for Doubly Ionized Beam

***Mass Efficiency Corrected for Backstreaming Neutral Atoms

Three distinct cathode operational modes were observed as a function of xenon gas flow during source "mixed mode" tests: high, normal and low cathode gas flow modes. The high gas flow mode appeared at cathode flow rates greater than 0.050 to 0.060 ampere equivalent flows. It was characterized by a low efficiency, high impedance and high applied potential discharge operation. Typically, a discharge potential of 60 plus volts was necessary to ionize 10 to 30 percent of the total mass flow in a 50 ohm discharge. Increases in the cathode xenon flow had no effect on the discharge impedance but did have some influence on the level of extracted beam. Changes in the main flow had no effect on the beam level until it was reduced to less than 0.100 ampere equivalent. Zero main flow reduced the extracted beam by 25 percent, and had no effect on discharge plasma impedance.

Argon-like source performance was observed in the normal gas flow mode during xenon cathode flows of 0.015 to 0.040 ampere equivalent. Discharge potentials between 47-60 volts were necessary to ionize 65-77 percent of the total mass flow in a 10-15 ohm plasma.

During the low cathode flow mode classic cathode keepr "plume" mode operation was observed. This is defined by extinguishment of the main discharge and a low current high potential keeper discharge. The above operational modes are probably related to cathode geometry phenomena and could be modified by changes in the cathode structure.

Operational difficulties prevented mixed mode testing with argon cathode flow and xenon main flow.

3.2.4 XENON OPERATION

Ion source operation with xenon achieved 94 percent mass utilization efficiency (corrected) at 254 eV/ion (see table 3-3). Xenon performance was found to be much less dependent upon the placement of the

TABLE 3-3

XENON OPERATION

D.P.	B. V.* (Volts)	j+ (Amps)	B. V.** (Volts)	j- (Amps)	Arc		Keeper		Cathode Mass Equiv. (Amps)	Total Mass Equiv. (Amps)	eV*/ion	eV**/ion	% Double Charged	Mass*** Eff. (%)
					Voltage (Volts)	Current (Amps)	Voltage (Volts)	Current (Amps)						
Chamber Pressure 6.2 x 10^{-5} torr - Backstreaming Neutral Ingestion 0.0426 amp Equivalent														
1600	1100	.490	320	.006	42	2.5	11.0	0.250	.035	.481	222.	225.	2.2	90.6
	1100	.510	320	.009	44	3.1	9.0	0.260	.035		276.	284.	4.7	92.8
	1100	.540	300	.010	49	3.6	9.0	0.260	.035		337.	367.	10.8	95.3
	1000	.455	300	.006	40	2.2	11.5	0.250	.035		202.	203.	1.0	84.0
Chamber Pressure 6.6 x 10^{-5} torr - Backstreaming Neutral Ingestion 0.045 amp Equivalent														
1405	1200	.660	600	.014	40	4.0	11.0	0.300	.037	.634	253.	254.	1.0	94.3
		.685		.015	45	4.3	10.0	0.300			293.	302.	6.0	95.3
		.710		.016	50	4.5	9.0	0.300			329.	350.	12.0	95.6
		.610		.012	37	3.6	12.0	0.30			228.	228.	0.0	87.2
		.640		.012	40	4.0	11.5	0.300			260.	261.	1.0	91.5
	1080	.635	600	.014	39	4.0	11.0	0.300			256.	256.	0.0	90.9
Chamber Pressure 2.5 x 10^{-5} torr - Backstreaming Neutral Ingestion 0.017 amp Equivalent														
1440	640	.300	300	.005	43	2.2	16.0	0.300	.043	.312	336.	343.	3.5	87.4
		.300		.006	45	2.5	16.0	0.300	.043	.312	399.	411.	6.0	85.9
		.307		.010	48	4.15	10.0	0.300	.043	.312	680.	716.	9.6	85.0
	800	.280	300	.005	40	1.85	11.5	0.300			281.	283.	1.0	82.2
	600	.300	600	.008	43	3.20	11.0	0.300	.043	.312	482.	491.	3.5	86.5

*Discharge and Keeper Power Uncorrected for Doubly Ionized Beam
**Discharge and Keeper Power Corrected for Doubly Ionized Beam
***Mass Efficiency Corrected for Backstreaming Neutral Atoms

boundary anodes than argon. Xenon mass efficiencies of 90+ percent were achieveable with any boundary anode-baffle configuration tested. Anode position controlled the amount of energy required to achieve the high mass efficiency.

MESC ion source xenon operation resembled that of mercury in many respects. First, high mass utilization efficiency was achieved at relatively low eV/ion operation. Secondly, reasonable discharge plasma impedance required cathode-to-main flow rates of 7 to 10 percent for both xenon and mercury rather than 30 to 40 percent with

argon. Third, fairly uniform boundary anode current densities were recorded with all the anodes set at the same position from the discharge chamber walls. Current density variations of less than 1.45 to 1 were collected by 2, 3, 4, 5, 8, and 9 with the anodes set in the mercury operational position. Performance and axial current density uniformity improved slightly with the anodes set in the optimum argon performance configuration. By contrast, argon's greater mobility, smaller mass, and higher operational plasma temperature enhanced its discharge performance sensitivity to anode placement.

During argon operation, mass utilization and energy consumption were both a function of the boundary anode placement. These results implied the recombination ion wall losses were much more sensitive to the placement boundary anodes in the case of argon.

Figure 3-1 summarizes the best performance obtained during tests with the 12 cm MESC ion source.

3.3 COMPONENT PERFORMANCE

3.3.1 ELECTRODE PERVEANCE

The electrode system perveance was mapped at low and high density beam currents with argon and xenon. The results are shown in tables 3-4 and 3-5. Electrode perveance was mapped by establishing stable operation and reducing the positive high voltage 100 or so volts at a time. These were plotted on log-log graph paper and the knee of the curve through the points was defined as the electrode perveance.

The data presented in table 3-4 and 3-5 show two unusual features. In principle, it is possible to calculate an electrode systems perveance for any gas once it is known for one gas. The data show that

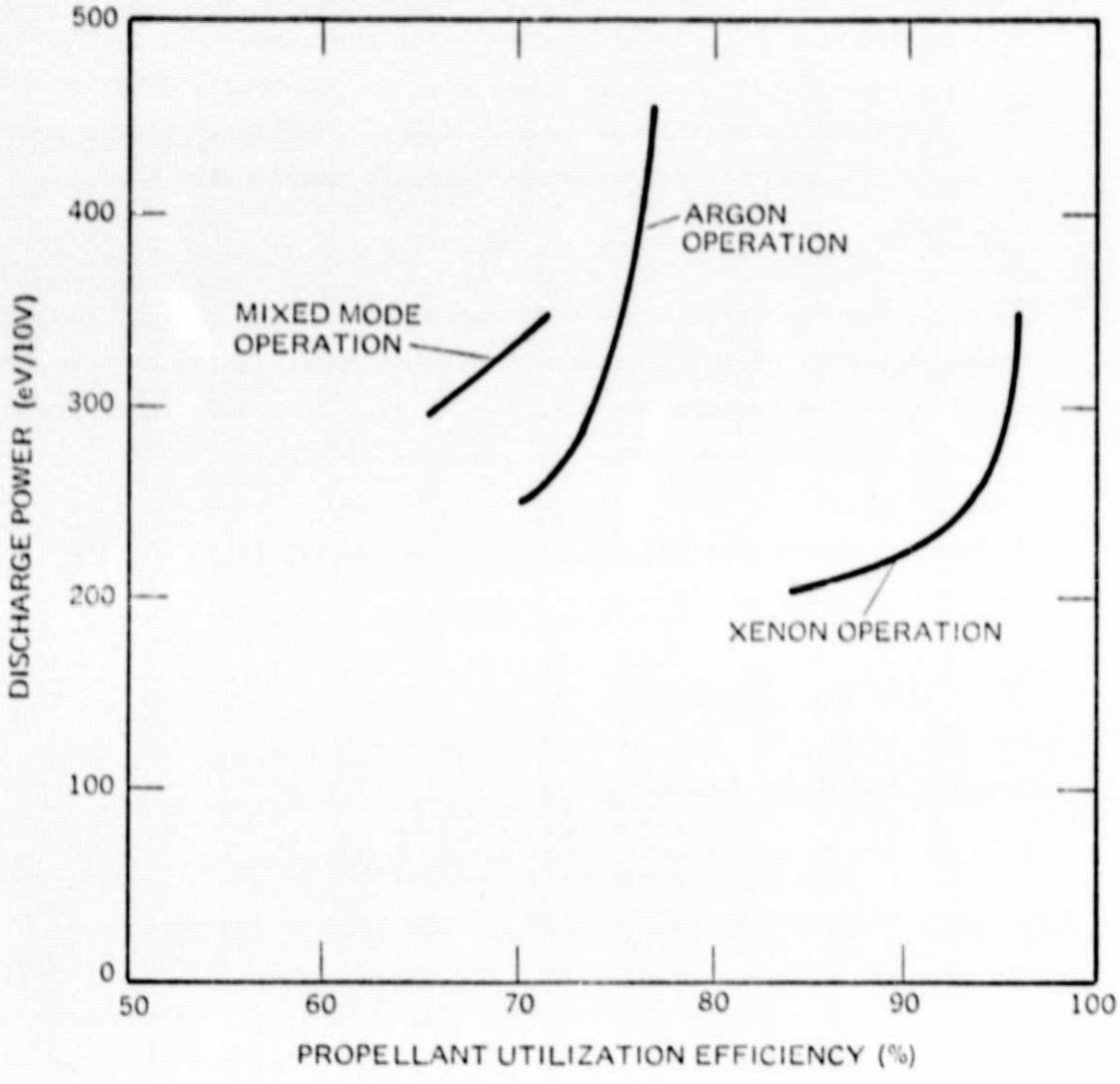

Figure 3-1. Ion Source Performance

TABLE 3-4

PERVEANCE DATA, ARGON OPERATION

D.P.	H. V.$^{+}$ (Volts)	J^{+} (Amps)	H. V.$^{-}$ (Volts)	J^{-} (Amps)	Arc		Keeper		Cathode Mass Equiv. (Amps)	Total Mass Equiv. (Amps)	Current Density (mA/cm^2)	Perveance/ Aperture (10^{-9})
					Voltage (Volts)	Current (Amps)	Voltage (Volts)	Current (Amps)				
10/10/77 - Chamber Pressure 3.0 x 10^{-5} torr - Backstreaming Neutral Ingestion 0.026 amp Equivalent												
1050	1000	.537	300	.007	53	3.35	9.0	.250	.355	.715	4.21	7.28
	900	.538	300	.009	53	3.35	9.0	.250	.355	.715		
	800	.538	300	.010	52	3.40	8.8	.250	.355	.715		
	740	.538	300	.015	53	3.41	8.8	.250	.355	.715		
	690	.540	300	.025	53	3.49	8.8	.250	.355	.715		
	670	.545	300	.045	52	3.60	8.8	.250	.355	.715		
10/10/77 - Chamber Pressure 4.0 x 10^{-5} torr - Backstreaming Neutral Ingestion 0.034 amp Equivalent												
1400	1200	.770	400	.011	52	3.40	10.0	.250	.244	1.043	6.02	7.79
	1000	.760	490	.011	52	3.40	10.0	.250				
	900	.760		.014	52	3.45	10.0	.250				
	800	.755	400	.020	52	3.47	10.0	.250				
	780	.760	400	.052	52	3.50	10.0	.250				

*Discharge and Keeper Power Uncorrected for Doubly Ionized Beam

**Discharge and Keeper Power Corrected for Doubly Ionized Beam

***Mass Efficiency Corrected for Backstreaming Neutral Atoms

TABLE 3-5

PERVEANCE DATA, XENON OPERATION

D.P.	H. V.$^{+}$ (Volts)	J^{+} (Amps)	H. V.$^{-}$ (Volts)	J^{-} (Amps)	Arc		Keeper		Cathode Mass Equiv. (Amps)	Total Mass Equiv. (Amps)	Current Density (mA/cm^2)	Perveance/ Aperture (10^{-9})
					Voltage (Volts)	Current (Amps)	Voltage (Volts)	Current (Amps)				
10/25/77 - Chamber Pressure - 6.6×10^{-5} torr Backstreaming Neutral Ingestion 0.030 amp Equivalent												
1405	1200	.640	600	.012	40	4.00	11.5	.300	.037	.614		
	1100	.640	600	.014	40	4.00	11.5	.300	.037	.614		
	1000	.630	600	.015	40	4.05					4.81	4.95
	900	.625	600	.017	40	4.05						
	800	.625		.037	40	4.10						
10/25/77 Chamber Pressure - 2.5×10^{-5} torr Backstreaming Neutral Ingestion 0.012 amp Equivalent												
	600	.300	300	.011	43	2.2	16.0	.300	.043	.312		
	500	.290	300	.011	43	2.2	16.0	.300			2.29	6.66
	400	.285	300	.015	43	2.2	16.0	.300				
	390	.300	300	.050	43	2.2	16.0	.300				

*Discharge and Keeper Power Uncorrected for Doubly Ionized Beam

**Discharge and Keeper Power Corrected for Doubly Ionized Beam

***Mass Efficiency Corrected for Backstreaming Neutral Atoms

this does not hold true here. Either the argon perveance is lower than it should be or the xenon greater. Changing the total flow from a high current density mode of operation to a lower one decreases electrode perveance in the case of argon and increases it with xenon. Both the phenomena can be explained as changes in the plasma distribution. Xenon has a more uniform plasma distribution when operating at low mass flows rather than at high. The inverse holds true for argon performance.

Early in the program the perimeter of the screen grid was masked to increase the discharge chamber pressure and reduce the plasma impedance. Masking was accomplished by spotwelding stainless shim stock to the upstream surface of the screen. Apparently the shim defocused the beamlets originating from the grid apertures next to it. This resulted in a radial elongation of the matching accel grid holes which changed from 1.17 mm circles to 1.17 by 1.4 mm ellipses. The erosion stopped with the removal of the mask. No other change in grid condition was noted.

3.3.2 CATHODE OPERATION

From the cathode operation or discharge current point of view source testing can be divided into two phases. The first phase was characterized by a high discharge plasma impedance with attendant low cathode emission currents. During this phase the cathode operated at emission currents ranging from 1.5 to 2.2 amperes with low mass utilization efficiency and incident cathode ion density. The cathode operated at temperatures calculated to be 1050 to 1150°C. No measurable erosion or weight changes were noted in the cathode or emitter or cathode orifice.

In the second cathode operational phase changes in the magnetic field and boundary anode position reduced the discharge plasma impedance and increased the cathode emission current to 2.5 to 4.0 amperes. A platinum-platinum rhodium thermmocouple was spotwelded to the side of the orifice plate in this phase and temperatures ranging from 1150 to 1290°C were seen. After several low impedance tests had been conducted, a hole developed in the tantalum delivery tube adjacent to the orifice plate. Microscopic examination found a white powder covering the inside of the tube close to the failure site. Further testing with another tantalum delivery tube produced a second tube failure. Estimated time to failure was about 50 hours.

The evidence indicated the tube failure was caused by emitter material overtemp operation producing tantalum oxidation. The tantalum tube was replaced with one of moly-rhenium in the next series of tests. No further evidence of erosion was observed in the 40 hours of testing completed since the change.

Operation at the temperatures associated with high emission currents may shorten the impregnated porous tungsten emitter lifetime. Comparing the emitter weights recorded before and after the 40 hours of tests indicated 20 percent of the barium aluminate had been lost. Future development should concentrate on reducing the emitter operational temperature.

3.3.3 BAFFLE CONFIGURATION OPTIMIZATION

The baffle disk diameter, the gap between the disk and the baffle housing tube, and the axial position of the assembly were optimized in testing. Diameters tested ranged from 0.95 to 1.30 cm with tube-to-disk gaps of 0.10 to 0.45 cm. The housing tube was moved 1.52 to 0.85 cm from the pole piece with each disk and gap configuration by means of the control rod described previously.

Tests found that optimum performance was obtained with a 1.11 cm disk located 0.16 cm from the tube, 1.24 cm from the pole piece. The axial optimum baffle position was found by relocating the structure until the minimum plasma impedance was observed.

Tests also discovered that the anode current distribution could be controlled by the baffle assembly axial position. Baffle movement either way from optimum reduced the current density differences between the anodes at the expense of mass utilization efficiency.

The various baffle disks were examined before and after each test. No evidence of baffle erosion was seen aside from a "shiny" appearance after one test at high discharge potential when the boundary anodes were located too far into the magnetic field.

3.4 TIME-OF-FLIGHT MEASUREMENTS

The percentage of double and single charged ions in the beam were deduced from time-of-flight data as a function of anode potential during ion source tests. Data were collected during quiescent discharge operation by short circuiting the extraction voltages and measuring the beam collector current as a function of time. Several scope traces were photographed at each discharge potential.

Figure 3-2 shows the typical traces recorded during an argon test. The percent of doubly ionized atoms in the ion beam was computed from the relative magnitudes of the signal representing the sum of double and single ion current and the signal representing singles alone. In some instances, trace noise was almost equal to the signal. In these cases, the average value of several traces were used to compute the percentage of double charged ions present. The values deduced were found to be comparable to those for the same anode potential reported earlier by Byers and Reader[4] (see table 3-6).

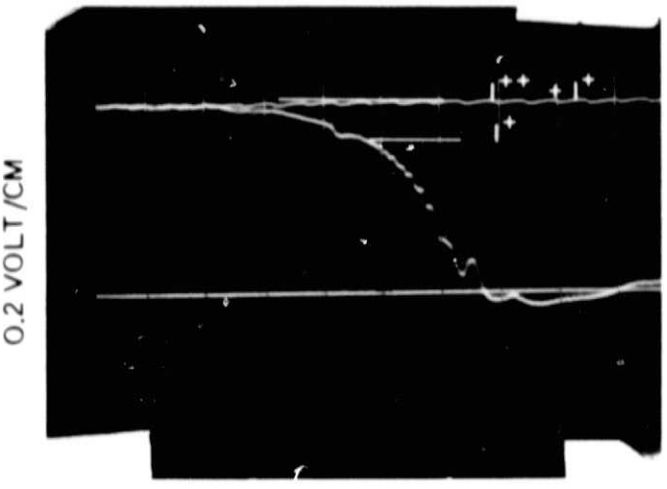

50 VOLTS ARGON
DISCHARGE
50μ SEC/CM SWEEP

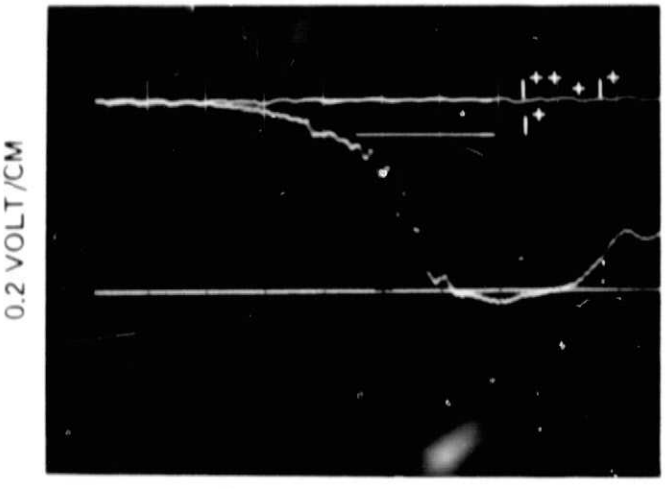

55 VOLT ARGON
DISCHARGE
50μ SEC/CM SWEEP

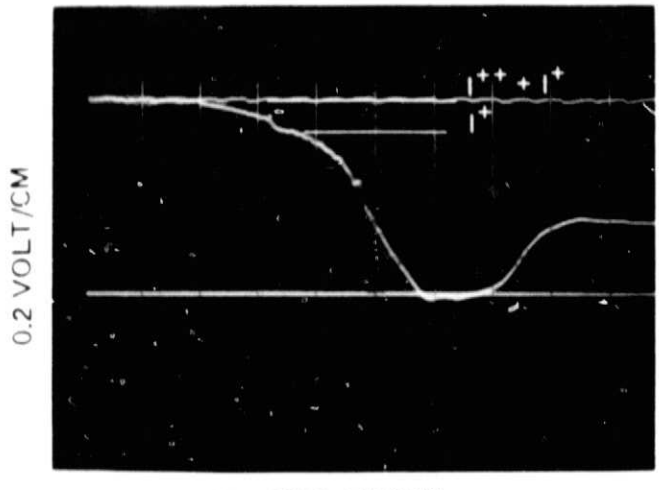

60 VOLT ARGON
DISCHARGE
50μ SEC/CM
(50 MICROSECONDS SWEEP)

Figure 3-2. Time-of-Flight Oscilloscope Traces

TABLE 3-6

TIME-OF-FLIGHT DATA

Discharge Potential	Percent Double Ionized Current (T.O.F.)	Percent Double Ionized Current (Byers and Reader)
50	5.2	5.3
55	5.1	6.2
60	7.9	7.5

3.5 BEAM DIAGNOSTICS

Beam flatness calculations were made from data collected 22 and 30 cm douwnstream of the accel grid with Faraday type beam probes. Two of the three probes used to measure ion beam distribution were cup probes located 22 and 30 cm from the accel and the third a 28 cm wide slit probe at 22 cm.

Beam width seen by the slit and cup probe agreed on all data taken. However, the beam density distribution differed. Argon and xenon data of both cup probes indicated the peak exhaust beam current density occurred at points 3.2 cm either side of the ion source center line. A xenon data trace, seen in figure 3-3, showed two maxima, one 2 percent greater than the other, with the beam central region density 6 percent less than their average, which was in good agreement with Langmuir probe data from the same test. The slit probe trace did not show a "hollow" beam but the ion current density maxima did occur 4 degrees off center in the same direction as the greater of the maxima.

Beam flatness calculations using the greatest current density and 99 percent of the collected beam found a 0.400 ampere argon beam had a flatness ratio of 0.515 and 0.530 at 22 and 30 cm, respectively. A second argon test with 0.649 ampere corrected beam had a flatness

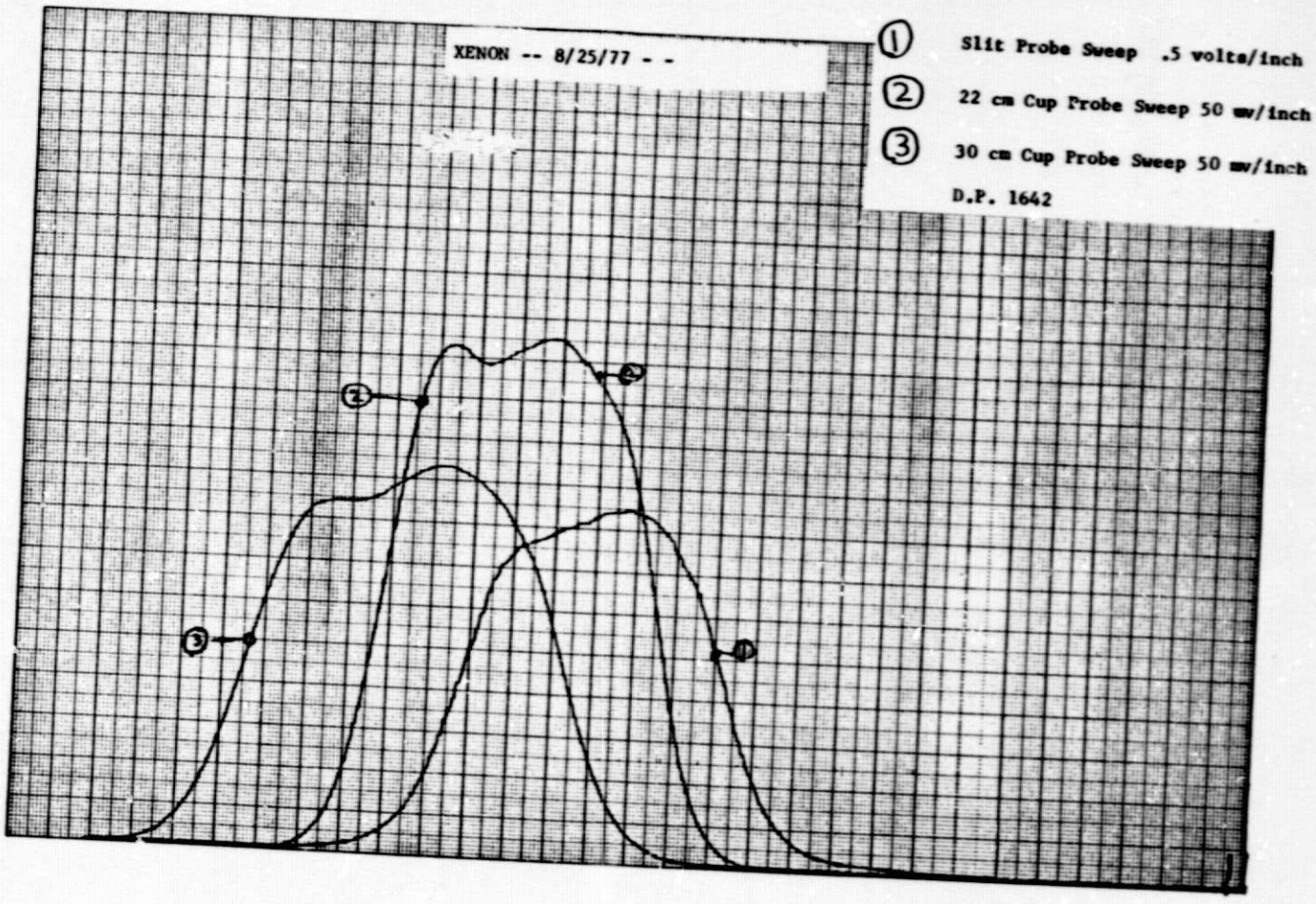

Figure 3-3. Beam Profile

ratio of 0.576 and 0.585 for the near and far probes with electrode potentials of 900 and 400 volts. If 95 percent of the collected beam was used instead, the calculated flatness increased to 0.691 and 0.711 for the 0.649 ampere beam. Xenon beam flatness was calculated from data collected during 0.404 ampere test with screen and accelerator potentials of 9C. volt and 400 volt, respectively. Using 99 percent of the collected beam, flatness was found to be 0.657 and 0.677 at 22 and 30 cm, respectively. Repeating the calculations for the same data trace using 95 percent of the collected beam found a beam flatness of 0.763 and 0.784 at 22 and 30 cm from the accel. The data presented above indicated a fairly uniform beam cross section for the noncompensated ion optics used in source testing.

3.6 DISCHARGE PLASMA DIAGNOSTICS

Langmuir probe data were plotted on semi-log and cartesian graphs and evaluated using the method described by Strickfaden and Geiler.[16] In this approach the second derivative of the linear graph was derived by construction and used to separate the energies and densities of the Maxwellian and primary electron populations. Figure 3-4 displays the graph of data collected during a 53 volt argon test and the curve derived from the linear graph of the same data. Plasma characteristics derived from the 53 volt argon test are presented in table 3-7 and the Maxwellian distribution is shown in figure 3-5.

Table 3-7 lists the electron density values used to produce figure 3-5 along with other operational characteristics of the plasma derived by the same method. Primary electron energy was found to always be negative of the applied anode potential with a density approximately one-third that of the Maxwellian electrons. The derived plasma or space potentials were found to be negative with respect to the anode potential in all cases.

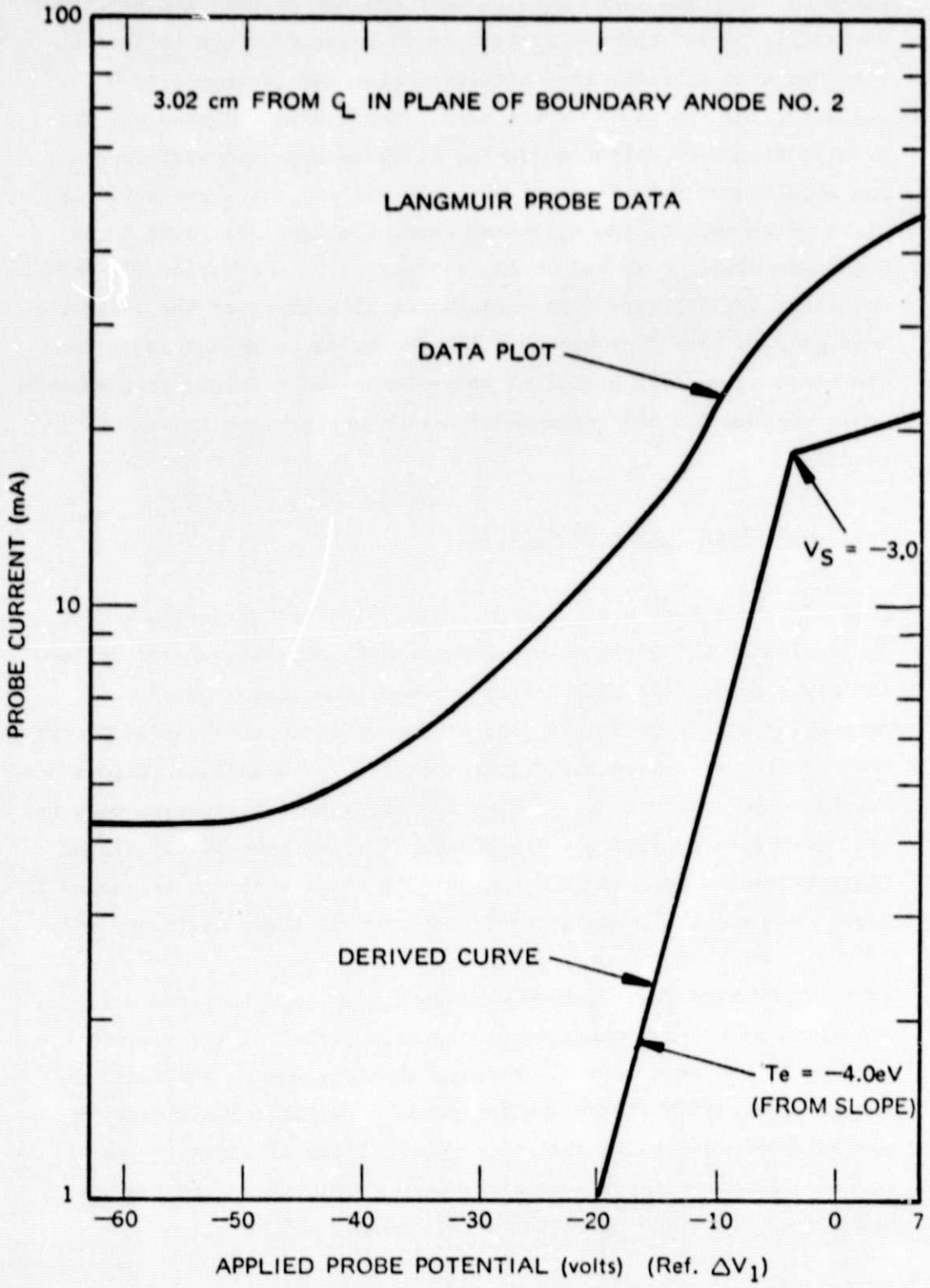

Figure 3-4. Langmuir Probe Test Datagraph

61404

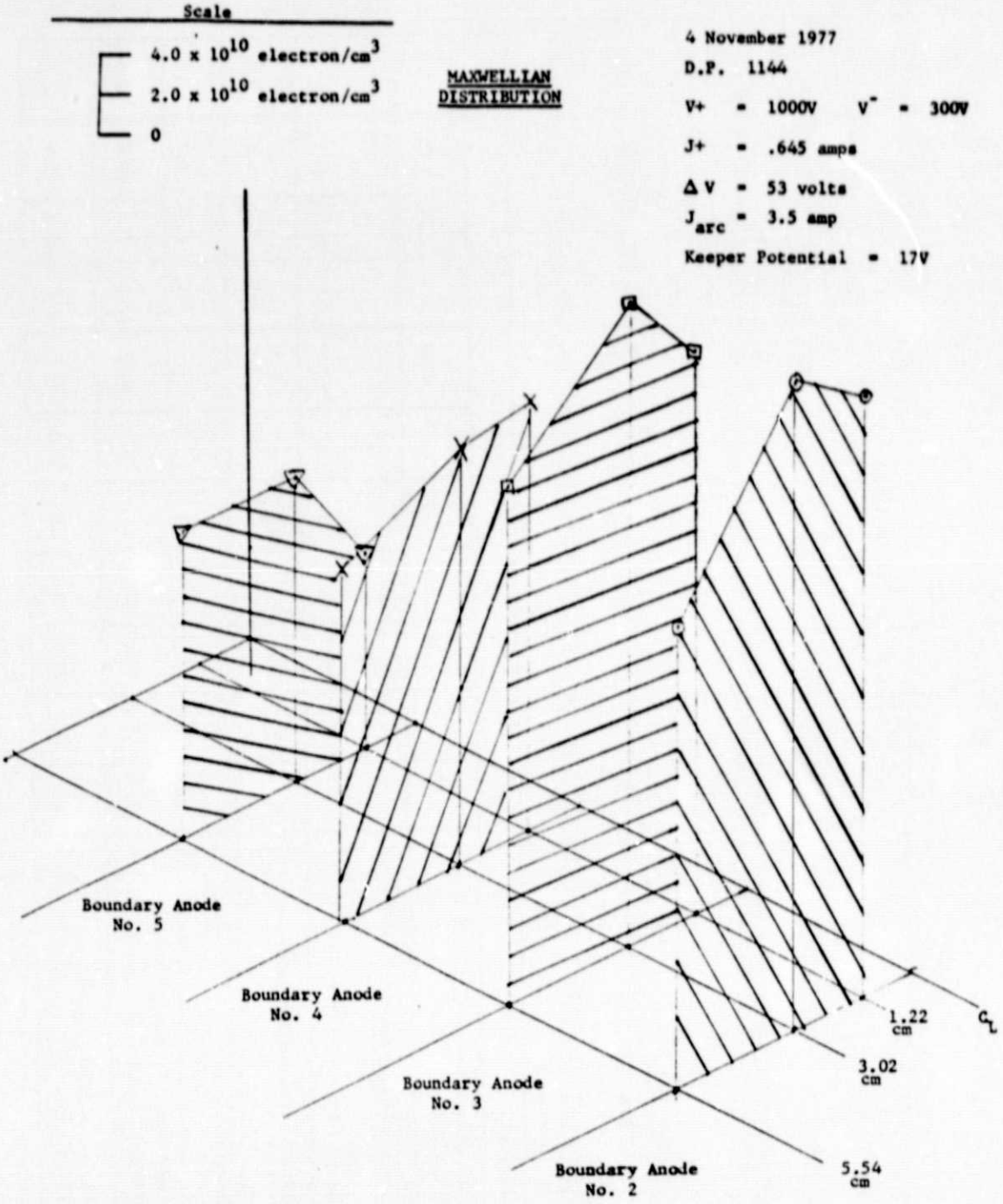

Figure 3-5. Maxwellian Distribution,
Cathode Mass Flow = 0.15A

TABLE 3-7

LANGMUIR PROBE DATA

Date	4 November 1977
D.P.	1144
Anode Potential (V)	53
Cath $\dot{m}$ (Amp equiv.)	.155
Main $\dot{m}$ (Amp equiv.)	.752

ANODE NO.	2			3			4			5		
Displacement from Centerline (cm)	1.22	3.02	5.54	1.22	3.02	5.54	1.22	3.02	5.54	1.22	3.02	5.54
ELECTRON PARAMETERS												
Primary Energy (eV)	47	47	45	47	47	46	48	38	40	41	41	45
Primary Density $\left(\frac{\text{electron}}{\text{cm}^3}\right) \times 10^{10}$	6.4	7.0	5.0	5.0	7.0	5.6	5.0	5.0	4.0	3.0	4.5	3.0
Maxwellian Energy (eV)	3.8	4.0	4.0	4.4	4.0	4.0	4.6	4.2	4.0	5.4	5.75	4.0
Maxwellian Density $\left(\frac{\text{electron}}{\text{cm}^3}\right) \times 10^{10}$	19.8	21.2	15.1	14.5	21.2	17.0	14.1	14.0	12.0	7.3	10.6	9.0
Ion Density $\left(\frac{\text{ion}}{\text{cm}^3}\right) \times 10^{10}$	26.2	28.2	20.1	19.5	28.2	22.6	19.1	19.0	16.0	10.3	15.1	12.0

The Maxwellian electron density depicted in figure 3-5 showed axial and radial variation which were typical of most moderate impedance argon plasmas measured. Axially, the maximum electron density went from 2.12×10^{11} in the plane of anode number two to 0.73×10^{11} electron/cm^3 in the plane of number five. Radial variation in electron density were seen in the plane of each anode. In the plane of the second anode, closest to the extraction grids, the maximum density occurred 3.02 cm from the discharge chamber center line and was 7 percent greater than the density closer to the axis and 40 percent greater than the density directly upstream of the outermost extraction grid holes.

Table 3-8 and figure 3-6 show the plasma operational qualities derived from a second argon test with 1.37 times the cathode mass flow of the previous test. Increases in the cathode mass flow produced reductions in discharge impedance and in Maxwell and primary electron energies and densities. Plasma potentials were found to be negative of the anode potential in all measurements.

Langmuir probe test results uncovered several interesting features of MESC discharge operation. The axial plasma density gradient seen in both tests discussed was found to be in fair agreement with a gradient calculated from the MESC diffusion current relationship and associated anode magnetic fields. It was pointed out in an earlier section, different magnetic fields were needed to attain a uniform electron current density to the boundary anodes. Using these fields and their respective diffusion currents, it was possible to calculate the plasma densities close to the anodes. The ratio in the densities between anode number two and anodes three, four, and five were found to be 0.85, 0.73, and 0.64. Using the result derived from the Langmuir probe data collected 5.54 cm from the centerline in the plane of the same anodes, the electron density ratios were 1.13, 0.79, and 0.60. The ratio of electron density was assumed approximately equal the plasma density.

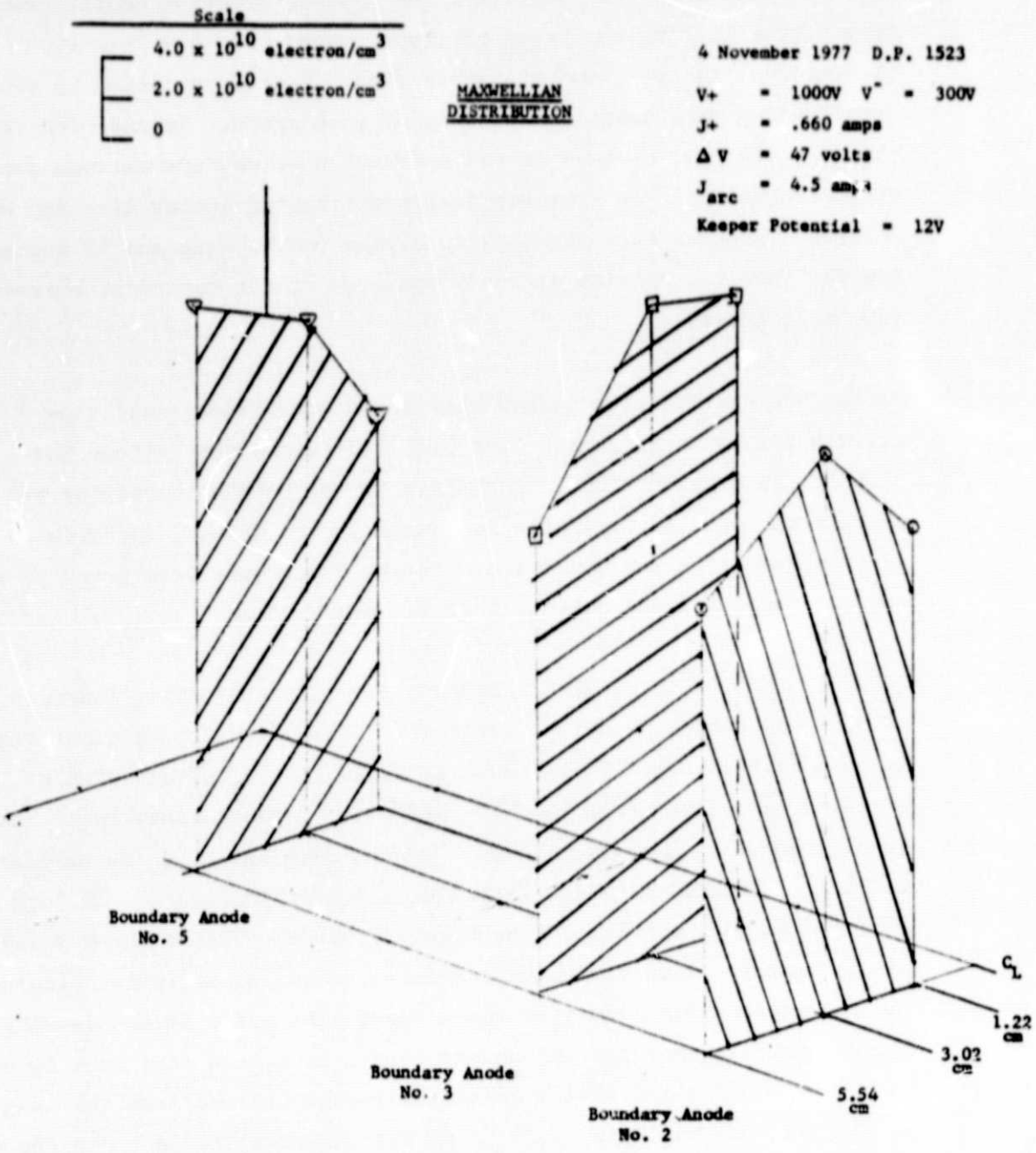

Figure 3-6. Maxwellian Distribution, Cathode Mass Flow = 0.21A

TABLE 3-8

LANGMUIR PROBE DATA

Date 4 November 1977

D.P. 1523

Anode Potential (V) 47

Cath $\dot{m}$ (Amp equiv.) .212

Main $\dot{m}$ (Amp equiv.) .725

ANODE NO.	2			3			5		
Displacement from Centerline (cm)	1.22	3.02	5.54	1.22	3.02	5.54	1.22	3.02	5.54
ELECTRON PARAMETERS									
Primary Energy (eV)	40	44	45	43	40	42	44	45	46
Primary Density $\left(\frac{\text{electron}}{\text{cm}^3}\right) \times 10^{10}$	5.2	5.6	4.7	6.3	1.7	4.8	3.7	5.1	6.0
Maxwellian Energy (eV)	3.45	3.0	3.8	3.2	3.3	3.4	3.0	3.0	2.8
Maxwellian Density $\left(\frac{\text{electron}}{\text{cm}^3}\right) \times 10^{10}$	15.6	18.2	14.3	20.3	21.0	14.8	12.6	17.5	18.2
Ion Density $\left(\frac{\text{ion}}{\text{cm}^3}\right) \times 10^{10}$	20.8	23.8	19.0	26.6	22.4	19.6	16.3	22.6	24.2

As noted on the previous page the plasma density in the central region was slightly lower than a point half way between the discharge chamber central region and the outside holes in the ion optic grids. The "hollow beam" profile was partly confirmed with Faraday probe measurements. The trace of the beam cross section collected by a cup probe found peak current density occurred at points either side of the beam centerline. Comparing the plasma characteristics and beam profile of the same test found the plasma center-to-peak density varied by 7 percent and the beam current density by 6 percent. However, the peak plasma density occurred 3.02 cm from the centerline and the peak beam current 3.84 cm from the centerline 22 cm downstream of the accel or an implied 2 degree half-angle spread.

The average-to-peak beam current density and ion density were calculated from data collected during the 53 volt argon discharge test discussed previously in this section. These calculations found the flatness ratio of the beam current density was 0.70, 22 cm downstream of the accel grid and the flatness ratio of the ion density was 0.88 in the plane of the second anode. Assuming the ion density distribution was similar to that at the screen grid 2.0 cm further downstream this implies a much flatter beam profile could have been realized by using compensated optics.

Plasma probe test results found the plasma potential was a few volts negative of the anode throughout the volume in which data were collected. This was first hypothesized by Moore[7] in the original derivation of the MESC concept. He showed plasma viscosity interaction of the MESC design produced a discharge plasma a few volts negative of the applied anode potential. This reduced recombination losses by reflecting more ions from the plasma boundary back into the discharge.

SECTION 4

SUMMARY AND CONCLUSIONS

The inert gas ion source program conclusively demonstrated that the MESC discharge chamber design is capable of efficient operation with either of the two gases tested. Under this program greater argon and xenon mass utilization were achieved at lower eV/ion than has been previously reported in the published literature.

Improved source performance was achieved by optimizing boundary anode position and the baffle disk geometry and using SHAG state-of-the-art optics. The 12 cm MESC discharge chamber used for these tests was converted from mercury to inert gas operation by relocating the boundary anodes as indicated by MESC theory and by changing the cathode baffle geometry. Argon was used for optimization as argon discharge performance was found to be the more sensitive to anode placement. After optimization, tests were conducted with xenon alone and with xenon and argon in mixed mode, where argon was fed through the main feed and xenon through the cathode.

Several probes were used to measure beam current profile and discharge chamber plasma characteristics. Faraday cup beam probes traversed the beam envelope 22 and 30 cm downstream of the accel grid. Probe position and ion current signals were recorded with a x-y plotter. Plasma characteristics were measured point-by-point by a Langmuir probe in the plane of the four anode structures.

Double and single charged components of the exhaust beam were determined with a time-of-flight collector. The collector measured the time required for an interruption in the ion beam to travel from the ion source to the collector. Double and single charged ion current

velocity differences were used to determine the percentages of each present in the beam.

Preliminary cathode tests in a small vacuum system were used to evaluate several inert gas cathode designs. Emphasis was placed on developing reliable electrical isolation of the keeper hardware and achieving maximum cathode electron emission current at minimum mass flow and temperature. Tests were conducted with 3.2 mm diameter cathodes using orifice diameters ranging from 0.36 to 0.64 mm. Long term keeper isolation was enhanced by masking the insulator surfaces from the keeper discharge region.

Cathode electron emission current in spot mode was found to increase with argon gas flow rate. This operational relationship was independent of orifice diameter. Gas flow rates produced the same emission current in all orifices tested. Changes in orifice diameter affected the flow rate necessary to achieve spot mode or to initiate discharge. The orifice size also affected the operational temperature observed at different emission currents. Test results showed cathodes functioned as a classic blackbody radiator where the orifice area was inversely proportional to the fourth power of temperature. For a particular orifice diameter, the cathode operational temperature was directly proportional to the electron emission. These temperature-emission current relationships were confirmed with an ion source cathode test.

Ion source performance was optimized by changing boundary anode position and baffle disk geometry. Argon mass utilization efficiencies of 65 to 77 percent were achieved at keeper-plus-main discharge energy consumptions of 200 to 457 eV/ion, respectively. Xenon operation was found to be less sensitive to boundary anode placement and 84 to 96 percent mass utilizations at 203 and 350 eV/ion were achieved. Mixed mode performance of the ion source was similar to argon, producing 65 to 71 percent mass efficiencies at 297 to 346 eV/ion.

Different cathode to main feed ratios were necessary to achieve the desired plasma impedance at 10 to 15 ohms with the various gases. Argon operation needed a cathode flow rate 30 to 40 percent of the total while xenon and mixed mode required 7 to 10 percent.

The test data were corrected for double charged ions and neutral atom backstreaming. The backstreaming neutral flux was calculated from the kinetic theory of gases. The flux ingested into the discharge was the product of the open accel area and the flux incident on its surface. Without these corrections the mass utilization efficiency would appear to be 5 percent higher than the true value and the eV/ion would be reduced proportionally.

Ion beam profiles deduced from plasma and beam probe data showed the argon and xenon have fairly uniform crossections. Both argon and xenon were found to have average-to-peak plasma density ratios of .88 inside the discharge chamber. Beam flatness average-to-peak measured in the ion beam were found to average 0.70 for argon and 0.77 for xenon during the same tests. Use of compensated optics could be expected to increase the beam flatness further.

Since the 12 cm hexagonal chamber was developed 9 years ago improvements have been made in MESC design. Comparing cesium performance with this same hex chamber and a more advanced, hemispherical, MESC design of the same size found a 20 percent improvement in performance, thus a similar improvement could be expected using inert gases in the advanced discharge chamber.

Future development should stress the use of the more advanced design MESC chamber and explore the impact of producing a larger chamber with a more favorable surface-to-volume ratio.

REFERENCES

1. D. F. Hall, "Electrostatic Propulsion Beam Divergency Effects on Spacecraft Surfaces," Final Report, Volume II, JPL Contract No. 952350.

2. J. M. Sellen, Jr., et al, "Material Deposition Process for North-South Stationkeeping Ion Thrusters on Three Axis Stabilized Spacecraft," paper presented at JANNAF Meeting, Anaheim, CA, September 1975.

3. R. J. Schertler, "Preliminary Results of the Operation of a SERT II Thruster on Argon," AIAA No. 71-157.

4. D. C. Byers and P. D. Reader, "Operation of an Electron Bombardment Ion Source Using Various Gases," NASA TN D-6620.

5. H. R. Kaufman, "Experimental Investigations of Argon and Xenon Ion Sources," NASA CR-134845.

6. W. L. Owens, Jr., "A Noble Gas Ion Propulsion System," AIAA No. 73-1114.

7. R. D. Moore, "Magneto-Electrostatically Contained Plasma Ion Thruster," AIAA No. 69-260.

8. W. Ramsey, "12 Centimeter Magneto-Electrostatic Containment Mercury Ion Thruster Development," AIAA Paper No. 71-692, AIAA/SAE 7th Propulsion Joint Specialist Conference, Salt Lake, Utah, June 1971.

9. R. M. Worlock, E. L. James, R. E. Hunter, and R. O. Bartlett, "Cesium Bombardment Engine N-S Stationkeeping Experiment," IEEE Transactions, Volume AES-11, No. 6, November 1975.

10. E. L. James and W. P. Ramsey, "A Phototype 12 cm Cesium Ion Thruster for North-South Stationkeeping," AIAA 75-387, Electric Propulsion Conference, New Orleans, La., March 1975.

11. M. J. Mirtich and W. R. Kerslake, "Long Lifetime Cathodes for 30 cm Mercury Thruster," NASA TMX-73523, Lewis Research Center, Cleveland, Ohio, November 1976, and private communication.

12. J. S. Sovey, "Characteristics of a 30-cm Diameter Argon Ion Source," AIAA Paper 76-1017, Electric Propulsion Conference, Key Biscayne, Florida, November 1976 and private communication.

13. G. Aston, H. R. Kaufman, "The Ion-Optics of a Two-Grid Electron-Bombardment Thruster," AIAA 76-1029, Electric Propulsion Conference, Key Biscayne, Florida, November 1976.

14. Y. S. Touloukian, "Thermophysical Properties Research Center," Volume 1, Thermophysical Properties Research Center, Purdue University, 1967

15. Dushman, "Scientific Foundations of Vacuum Techniques," (Second Edition), 1962, John Wiley & Sons, pages 90-93

16. W. D. Strickfaden and K. L. Geiler, "Probe Measurements of the Discharge in an Operating Electron Bombardment Engine," AIAA Journal, Vol. 1, No. 8, August 1963, pages 1815-1825.

17. G. C. Isaacson and H. R. Kaufman, "Multiple Gas Thruster Design," NASA CR-135101, Colorado State University, Fort Collins, Colorado, June 1977.